SPACE VEHICLE CHEMICAL INTERACTIONS AND TECHNOLOGIES

Benjamin D. Prince and Raymond J. Bemish

26 May 2015

Final Report

APPROVED FOR PUBLIC RELEASE; DISTRIBUTION IS UNLIMITED.

AIR FORCE RESEARCH LABORATORY
Space Vehicles Directorate
3550 Aberdeen Ave SE
AIR FORCE MATERIEL COMMAND
KIRTLAND AIR FORCE BASE, NM 87117-5776

NOTICE AND SIGNATURE PAGE

//SIGNED//   //SIGNED//

_____   _____
Dr. Raymond Bemish   Glenn M. Vaughan, Colonel, USAF
Project Manager, AFRL/RVBXT   Chief, Battlespace Environment Division

REPORT DOCUMENTATION PAGE

1. REPORT DATE *(DD-MM-YYYY)*	2. REPORT TYPE	3. DATES COVERED *(From - To)*
26-05-2015	Final Report	01 Oct 2007 – 30 Sep 2014

4. TITLE AND SUBTITLE

Space Vehicle Chemical Interactions and Technologies

5a. CONTRACT NUMBER

5b. GRANT NUMBER

5c. PROGRAM ELEMENT NUMBER
61102F

6. AUTHOR(S)

Benjamin D. Prince and Raymond J. Bemish

5d. PROJECT NUMBER
2301

5e. TASK NUMBER
PPM00004270

5f. WORK UNIT NUMBER
EF004373

7. PERFORMING ORGANIZATION NAME(S) AND ADDRESS(ES)

Air Force Research Laboratory
Space Vehicles Directorate
3550 Aberdeen Avenue SE
Kirtland AFB, NM 87117-5776

8. PERFORMING ORGANIZATION REPORT NUMBER

AFRL-RV-PS-TR-2015-0110

9. SPONSORING / MONITORING AGENCY NAME(S) AND ADDRESS(ES)

10. SPONSOR/MONITOR'S ACRONYM(S)

AFRL/RVBXT

11. SPONSOR/MONITOR'S REPORT NUMBER(S)

12. DISTRIBUTION / AVAILABILITY STATEMENT

Approved for Public Release; distribution is unlimited. (377ABW-2015-0452 dtd 09 Jun 2015)

13. SUPPLEMENTARY NOTES

14. ABSTRACT

This report details basic physics/chemistry associated with electrospray propulsion technology, plasma processes in Hall effect thrusters, optical signatures of xenon plasmas, hyperthermal collisions of xenon ions, charge exchange cross sections of ion-atom and ion-molecule processes, and interactions of ion-thruster propellants with atmospheric species. The effect of propellant flow rate on the electrospray thruster performance is emphasized and molecular dynamics simulations are used to provide fundamental underpinnings of the microscopic behavior of the emission process. Differential cross sections related to large angle scattering of xenon ions after elastic collision with neutral atomic xenon are measured and discussed with an emphasis on transitioning the results to the modeling community. Emission excitation cross sections of xenon ion-xenon atom collisions, krypton ion-atom collisions and electron-krypton collisions are reported for energies relevant to electric propulsion systems. Total charge exchange cross sections, branching ratios, and energy analysis of krypton ion-krypton atom collisions and iodine (molecular and atomic) ions with molecular iodine are presented for energies relevant to electric propulsion systems. Interactions between ion thruster propellants and ammonia and atomic oxygen ions and ammonia are presented.

15. SUBJECT TERMS

Electrospray, charge transfer, ion thruster, ammonia, xenon, iodine, ionic liquid, Taylor cone, electric propulsion, krypton, colloid, molecular dynamics, atomic oxygen, plasmas

16. SECURITY CLASSIFICATION OF:			17. LIMITATION OF ABSTRACT	18. NUMBER OF PAGES	19a. NAME OF RESPONSIBLE PERSON
a. REPORT	**b. ABSTRACT**	**c. THIS PAGE**			Dr. Raymond Bemish
Unclassified	Unclassified	Unclassified	Unlimited	70	19b. TELEPHONE NUMBER *(include area code)*

This page is intentionally left blank.

Table of Contents

List of Figures

List of Tables

This page is intentionally left blank.

1. INTRODUCTION

This report contains information about the research activities of the Space Chemistry Laboratory over the previous eight years covering the period of 1 Jan 2007 to 1 Jan 2015. The Space Chemistry Laboratory is a primarily 6.1-funded research group performing basic science measurements focused on the chemistry and fundamental physics of processes occurring in low-Earth orbit and greater altitudes. The group resides in the Space Vehicles Directorate, Battlespace Environment Division, Space Weather Center of Excellence Section. During the period covered in this report the laboratory has been located at Hanscom AFB in Massachusetts and Kirtland AFB in New Mexico.

This report consists of material that has been published in journal articles over the report period. The authors of this report have been responsible for some of the publications reported here but many of the publications were written by other authors. Citing of material within this report should also include the citation of the relevant paper whose information can be found in the introductory paragraph to every section in Section 4. In particular, the bulk of the material reported is focused on three distinct avenues of research effort. The first direction is the development of electrospray thruster technology through the investigation of the physics and chemistry occurring at the emission region. The second is through measurement of fundamental chemistry/physics of processes that occur in ion thrusters with a particular emphasis on xenon, krypton, and iodine propellants. The final area relates to the measurement of chemistry related to the spacecraft environment, with a particular emphasis on potential interactions between electric propulsion systems and the atmosphere or other propulsion systems.

2. BACKGROUND

With increasing international access to the space domain, our national security relies more heavily on our capability to operate, protect, detect and track space assets. As space technology continues to be miniaturized, we are challenged to improve our ability to monitor and respond to small space assets in real time. Such a capability will require detecting and predicting the signatures of spacecraft maneuvers, developing miniature satellites with flexible micropropulsion systems, novel miniature sensors, and new algorithms and models to identify hostile objects in space. Understanding the chemical and physical processes associated with operating in the space environment plays a key role in meeting these needs.

One of the nation's space situational awareness (SSA) challenges remains the prevention of tracking loss of spacecraft due to maneuvers. When a spacecraft maneuvers, optical signatures are produced from energized engine effluents and, at low-Earth orbit altitudes, from their energetic chemical interactions with the surrounding atmosphere. At higher altitudes, the interaction of engine effluents with solar radiation becomes important. The collision energies range from a few eV (hyperthermal energy), which occurs in the low-Earth orbit environment, to several keV, in the electric thruster environment. These highly non-equilibrium chemical interactions create vibrationally and electronically excited molecular species. Reaction dynamics theory continues to be validated with the increasing availability of high-quality experimental state-selected reaction cross sections. These cross sections are also important in numerous theoretical simulation methods for modeling of aerospace environments, such as the communications blackout of re-entry space vehicles.

Another challenge pertains to the increasing use of high-efficient electric propulsion systems in the space domain. Electric propulsion systems are high efficiency alternatives to chemical propulsion systems which result in significant launch weight savings. Approximately 90% of the lift-off mass of geosynchronous satellites is due to propellant mass for chemical engines, while xenon propelled Hall effect thrusters (HET) reduce the propellant mass fraction at lift-off to ~30%. In HETs, a precursor gas, most commonly xenon (Xe), is efficiently ionized in a discharge and the resulting ions are accelerated to high energies ranging from 0.2 to 2 keV to generate thrust. Ion thrusters have become a common propulsion system on satellites residing in geosynchronous orbit and are expected to become even more common in the coming decades.

The development and optimal integration of these high-specific impulse engines are critically dependent on correct and comprehensive modeling of the interactions of the HETs with their environment. A key part of the models is the physics of electron impact excitation/ionization and ion-neutral collision cross sections. Accurate elastic scattering, differential and charge-exchange cross sections of xenon ions colliding with xenon atoms are critical in properly modeling the Hall thruster plasma. Energetic ions contribute to a number of problems including insulator erosion in the discharge channel of these thrusters and sputtering of sensitive surfaces of the spacecraft. In the meantime, the xenon plasma produces optical signatures due to the collisional excitation of xenon by electrons and xenon ions.

The third direction of focus related to a relatively new type of electric propulsion system, commonly called "electrospray thrusters". The plasma based electric propulsion technologies described above have limited potential with respect to miniaturization. This is primarily because plasmas lose efficiency as the plasma surface-to-volume ratio increases upon size reduction. An alternative approach is a discharge-free, electrospray technology in which the charged particles are extracted with high electric fields from a conducting and low vapor pressure liquid. In essence, the electric field causes the liquid-vacuum interface to form a conical shape, called a Taylor cone, when the electric field is in balance with the surface tension of the liquid. At the tip of the cone, the electric field strength is very high causing the generation of a jet which eventually breaks up into charged droplets and/or ions. As the jet enters the nanometer dimension, leading to surface fields in excess of 1 V/nm, ion field evaporation becomes important. Microelectric propulsion technologies based on the electrospray principle include field emission thrusters that use metal liquids, and colloid thrusters, which are electrospray thrusters that employ organic liquid salt solutions as propellants. While field emission thrusters produce metal ions suitable for high specific impulse applications, electrospray thrusters have broader operating conditions comprising pure droplet, mixed ion/droplet, and pure ion modes. This allows tenability in the specific impulse and thrust of the electrospray thruster, which particularly advantageous for flexible mission planning needs.

In Section 3, we describe the experimental apparatus used to make the measurements detailed in this report. Section 4 contains the experimental and theoretical results over the period of performance. This section is broken into 15 components grouped such that the Sections 4.1 through 4.6 cover the electrospray propulsion research area, Sections 4.7-4.12 cover the Hall thruster physics research area, and Sections 4.13-4.15 cover the physics of the spacecraft environment research area. The research presented in each component of Section 4 has already been published in the scientific literature and the introduction paragraph of each section contains reference to the location of the article.

3. METHODS, ASSUMPTIONS, AND PROCEDURES

3.1 Experimental Apparatus and Methods for Electrospray Thruster Project

All reported experiments in this project area occurred in the Electrospray Thruster Mass Spectrometer instrument. This instrument is a high vacuum system consisting of two chambers with base pressures near 5×10^{-7} torr. The two chambers are broken into a "source" chamber consisting of the electrospray source and near field targets, as described below. The second chamber consists of a quadrupole mass spectrometer with a retarding potential analyzer and channeltron attached. Only general experimental details are presented here and readers are encouraged to consult the various publications for exact experimental details.[1-6]

The schematic of the experimental apparatus is presented in Figure 1. Each chamber is pumped with a 250 l/s turbo pumps backed by suitable mechanical pump. The left-most component is an electrospray source, either capillary or solid metal needle, mounted into a copper block. Offset approximately 1-3 mm is a metal plate with a 1.5-mm-diameter orifice that serves as an extractor plate that rotates with the source. The source and extractor are connected to two different high voltage pulsing power supplies that are triggered off of two digital delay generators in which the second delay generator is triggered off the master delay generator and the phase between the two units is manually controlled. The source is typically operated at +/- 500 V for cation and anion emission, respectively, generating ions with kinetic energies equal to 500 eV or less. The extractor is typically operated between -/+500-1900 V for cation and anion emission, respectively. The polarities are typically alternated at a rate of 1 Hz.
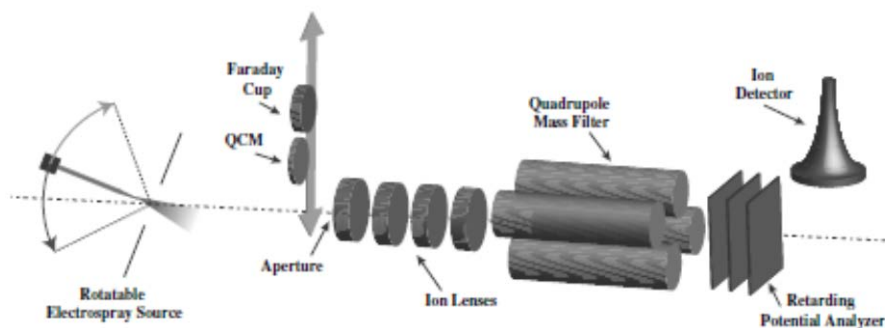
Figure 1: Experimental Apparatus for Electrospray Experiments

The source system is mounted on a gear system that allows +/- 45 degree rotation controlled outside the vacuum system. The entire flange is mounted onto an XY stage that allows the emitter to be positioned exactly down the center axis of the instrument (dotted line in Figure 1). When operating with a metal needle source, as in the case of Figure 2, the ionic liquid is applied externally to a crossbar that has been physically mated to the needle and acts as a reservoir for the experiment. Alternatively, an electrically conductive capillary of tip size 50-100 μm is connected to suitable transport capillary and immersed in a reservoir outside of the apparatus containing the chemical mixture of interest. This mixture is driven through the capillary through the use of a pressure regulation system that will be detailed below.
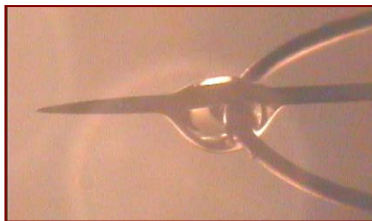
Figure 2: Example Externally Wetted Tungsten Emitter Tip with IL Applied

After successful electrospray of the liquid occurs with suitable potentials being applied to the source and extractor, the emitted species are interrogated with a pair of near-field tools. A Faraday cup (FC) consisting of a grounded grid and metal plate and a quartz crystal microbalance (QCM, Inficon) equipped with a gold crystal are mounted onto a translation stage that allows manipulation from outside the apparatus. This stage is offset approximately 18 mm behind the extractor. The FC is electrically connected to an electrometer operating in current sensing mode and measures the total current impinging on the plate. The output of the QCM is electrically connected to a local oscillator connected to a control unit (Inficon) which measures the thickness rate, related to the mass flow rate, of material that impinges on the crystal service. The third position on the translation stage is a simple optical element that allows the emitted ions access to the second chamber of the apparatus. Generally, both the QCM and FC have plates with apertures of 6 mm allowing ion access to the units.

The second chamber consists of optical elements designed to improve throughput into the quadrupole mass spectrometer. This quadrupole mass spectrometer is connected to suitable RF and DC power supplies and allows mass-to-charge (m/q) selection when operational. Ions are counted by means of an off-axis ion detector (channeltron) operated at suitable voltages depending on cation or anion detection. When the quadrupole is operated to allow an ion to pass, these ions encounter a three grid system that comprises a Retarding Potential Analyzer (RPA) capable of measuring the kinetic energy of passed ions. This system is operated by sweeping through all voltages applied to the second grid with the first and third grids grounded and monitoring the attenuation of ion counts on the channeltron.

The output of the channeltron is converted into usable signal by directing the signal out of the channeltron into two channels of a pre-amplifier. This amplified signal is directed into a signal discriminator. The output of the discriminator is directed onto a National Instruments Counter Card attached to a computer and simple counting of pulses serves to determine the number of ions. The ion counting, quadrupole m/q selection and RPA potential are all controlled through a custom computer program and data is output, manipulated and stored in this software.

In the experimental results involving the use of a capillary emitter source, the flow of the ionic liquid propellant is controlled through a pressure regulation system presented in Figure 3. Briefly, a N_2 supply cylinder introduces gas into the system which accesses the ionic liquid reservoir through a shutoff valve. This gas generates a pressure above the liquid in the reservoir that enables the liquid to be driven up the transport capillary into the experiment at some flow rate. The pressure above the liquid is monitored through the use of an MKS Pressure Transducer and associated readout unit. The system is actively pumped through a mechanical pump attached to the end of the pressure system. Not shown in Figure 3 is a shutoff valve that separates the reservoir from the pump. The pressure in the reservoir is controlled through a combination of the

Approved for public release; distribution is unlimited.

needle valve setting and the pressure setting of the second stage of the regulator attached to the N_2 supply.
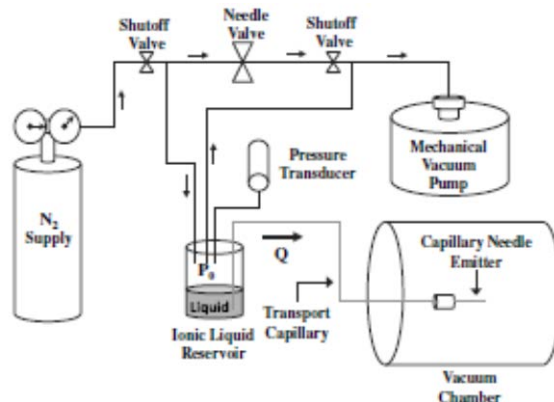
Figure 3: Capillary Fluid Feed System. Arrows Indicate Flow Path of Gas

3.2 Guided Ion Beam Apparatus

The Guided Ion Beam (GIB) apparatus is the first of two apparatuses used to explore ion thruster research and ion-molecule collisions. This system is described in brief detail below but readers are encouraged to consult the published material for full detailing of the experimental system and settings for each individual research event described in the results and discussion sections.[7-11]

The experimental apparatus is depicted in Figure 4. The instrument is broken into several distinct regions: source/ion generation, mass selection, double octopole, and quadrupole mass spectrometer. The apparatus is pumped by four different turbo pumps: a 250 l/s turbo pump below the skimmer, a 250 l/s turbo pump for the quadrupole mass spectrometer and the mass selection region and a 900 l/s turbo pump for the double octopole region. The base pressure of the system is approximately 10^{-8} torr for the quadrupole mass spectrometer and double octopole region, 10^{-7} for the source region and 2×10^{-6} for the mass selection region. Each of these turbo pumps is backed by appropriate mechanical pumps.

The source region is responsible for generation of the desired ion beam. This is accomplished through the use of a magnetically confined electron beam with user specified electron energy impacting on the gas of interest. Ions generated from electron impact pass through a skimmer and are directed into the mass selection region. The mass selection system is composed of an Einzel lens directing the ion beam into a quadrupole bender which bends the ion beam 90 degrees. A second Einzel lens directs the ion beam into a Wien filter (Colutron, Model G-2-D) where crossed electric and magnetic fields allow extraction of the desired ionic species.

The m/q selected ions are directed into a chamber equipped with a two-stage RF octopole ion guide separated by a reaction chamber and insertion and extraction lenses. The ions encounter the insertion lenses which slow the axial velocity of the ion beam to approximately 0.25 eV before entering the first stage of the octopole. Upon entering the octopole, the ions are accelerated to the desired kinetic energy before entering the reaction chamber where they encounter a target gas of interest. Any ions produced in this collision and the remnants of the primary ion beam enter the second octopole and are guided to the final detection chamber after

passing through a set of four extraction lenses. The detection chamber consists of a quadrupole mass filter and either an on-axis or off-axis channeltron for ion detection.

Ion counting occurs through directing the output signal cable of the channeltron into two channels of a pre-amplifier. The output of the 2nd channel of this pre-amplifier is directed into a discriminator. The output of the discriminator is split and directed into a ratemeter for optimization and the second leg is directed into a National Instruments counter card that counts pulse events and transfers the output to a local computer. This computer system is equipped with custom software designed to control the quadrupole mass spectrometer, octopole DC voltage, and ion counting and various analysis routines for processing the data.

Several operational modes exist for this instrument including the attenuation mode, time-of-flight mode, and branching ratio mode. In the attenuation mode, the m/q value of the primary ion is monitored on the quadrupole while the target gas is introduced at single collision pressures. The first octopole DC voltage is set to generate the desired kinetic energy of the primary beam. The second octopole DC voltage is set approximately one volt higher which prohibits thermal and near-thermal ion products from entering the second octopole. The number of ions is counted in the presence and absence of the target gas and converted to a cross section through suitable manipulation, as described in each text.

The apparatus can also operate in time-of-flight mode through pulsing of a deflector preceding the first stage of the octopole ion guide. In this operational mode, a short 2 µs gate pulse generated from a digital delay generator and arbitrary waveform generator on the deflector allows ions into the octopole ion guide and reaction chamber. Generated ions of any mass are extracted into the second stage of the octopole ion guide through the application of a ring electrode at the entrance to the reaction cell at ~100 V, which generates a penetrating field of a few tenths of volts that reflect slow, backscattered, thermal products, and through the setting of the second octopole DC potential 0.4 V below the first octopole. The flight time of every ion of interest is recorded and is converted to product kinetic energy.

In the branching ratio operational mode, all products of interest are sequentially mass selected and their relative ion counts recorded at the ion specific optimal extraction voltages. The second octopole is held 0.4 V below the first stage and no gating is employed. This mode allows the determination of the relative weighting of all charged products regardless of kinetic energy.
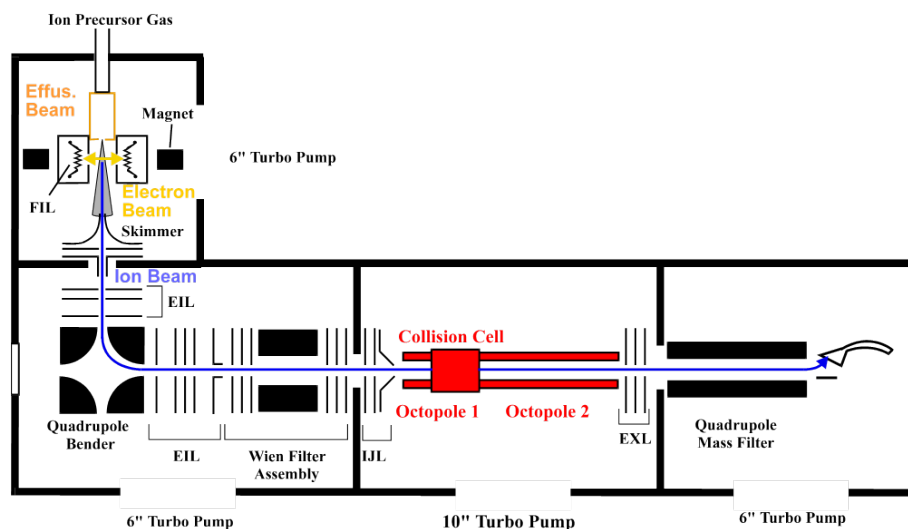
Figure 4: Schematic of Guided-ion Beam Apparatus

3.3 Ion-Neutral Chemi-Luminescence Detector

The Ion-Neutral Chemi-Luminescence Detector (INCLUDE) apparatus was used to investigate both the ion thruster and ion-neutral collision project areas of this report. This system is described in brief detail below but readers are encouraged to consult the published material for full detailing of the experimental system and settings for each individual research event described in the results and discussion sections.[12-15]

This apparatus, depicted in Figure 5, is composed of three distinct regions: the source, mass selection, and reaction chamber. The source region and mass selection region are actively cooled with kerosene liquid at approximately 12 ^{o}C to equilibrate the temperature of the source region and the magnet used for the mass selection. The entire apparatus is pumped with two turbo pumps; a 250 l/s pump and a 700 l/s pump. Both turbo pumps are backed by suitable mechanical pumps operating at 5-50 millitorr. The base pressure in the source chamber is approximately 2 x 10^{-7} torr and the reaction chamber is approximately 5 x 10^{-8} torr in the absence of any input gases.

The source region is a DC discharge source in which a source gas is flowed into a chamber, typically around 100 millitorr, and a large current is applied to a filament resulting in electrons that are rapidly accelerated towards an anode held at an energy specified by the user relative to the filament. A wide variety of ions and charges are generated from collision of these electrons with the source gas. These ions are accelerated into a Wien filter (Colutron, G-2-D) where crossed electron and magnetic fields separate the ion trajectories. After user selection of the ion of interest, the ions exit the mass selection region by traversing an ion decelerator (Colutron) which sets the kinetic energy of the ions to the desired value. Once through this decelerator, the ions are introduced into the reaction chamber where several optical elements allow optimization of the beam.

Once beyond the optical elements, this beam then encounters a cubic reaction cell (2.54 cm x 2.54 cm x 2.54 cm) with a 1.5 mm aperture on the front surface of the cell. The back end of this cell has the same aperture and allows the ion beam to pass through to a series of grids capable of acting as an RPA before colliding into a FC which directly interrogates the current of the ion beam. The FC is electrically isolated from the chamber and the output is directed onto an electrometer operating in current sensing mode. In addition to the FC used for current measurement, the back wall of the cell is also electrically isolated from the chamber and the output of this element is connected to a second electrometer, also set to current sensing. Besides the entrance and exit apertures of the reaction cell, two gas inlet lines are attached to the side of the cell to allow for target gas entrance and pressure measurement. On the top of the cell, looking down into the interaction region, is a fiber optical bundle that accepts light generated inside the reaction cell. The other end of this bundle is directed out of the vacuum chamber and the output of the fiber is introduced into a spectrograph with an attached charged-coupled device (CCD) camera. This spectrograph breaks the light into its component wavelengths before impinging on the camera pixels. This camera is directly attached to a local computer and data is transferred, processed and stored via software control of the camera.

Processing of the data involves removal of background and cosmic rays in addition to multiplication of the output signal by the spectral response of the detection system. This response is calibrated by measuring the spectral output of a tungsten lamp operating at ~2100 K, whose temperature has been measured by a calibrated pyrometer. This measured optical

spectrum of the lamp is compared against an ideal blackbody of the same temperature and a wavelength specific correction curve is generated. After correction, the outputted counts are converted into counts/second and the wavelength specific cross section is given by:

$$\sigma_\lambda = \frac{J_\lambda eq}{GPI} \tag{1}$$

where J_λ is the counts/second of the spectral transition, e is the electron constant, q is the ion charge, P is the pressure of the target gas, I is the total ion beam current and G is a geometric factor that is obtained by comparison of measured values against a standard system. In practice, spectrographs and CCD detectors do not generate signals that are one pixel wide, so J_λ is often an integral over some number of pixels associated with a specific transition. These cross section values are tabulated for every transition of interest and are typically generated for a number of different kinetic energies of interest.

In addition to the ion-neutral collisions that have been described above, occasionally the cross sections resulting from electron impact onto a target gas is of importance. In this case, only the reaction chamber component of the apparatus is of interest. Everything from the reaction cell back to the FC is unchanged but instead of using a DC discharge source, an electron gun and associated optical elements is attached a small distance in front of the first cell aperture. The electron gun is operated at approximately 30 µA total emission current at a specified electron energy and the resulting electrons are steered and introduced into the collision cell where the light is monitored with the same fiber optic. The analysis is completely identical to that of the ion-molecule collisions.
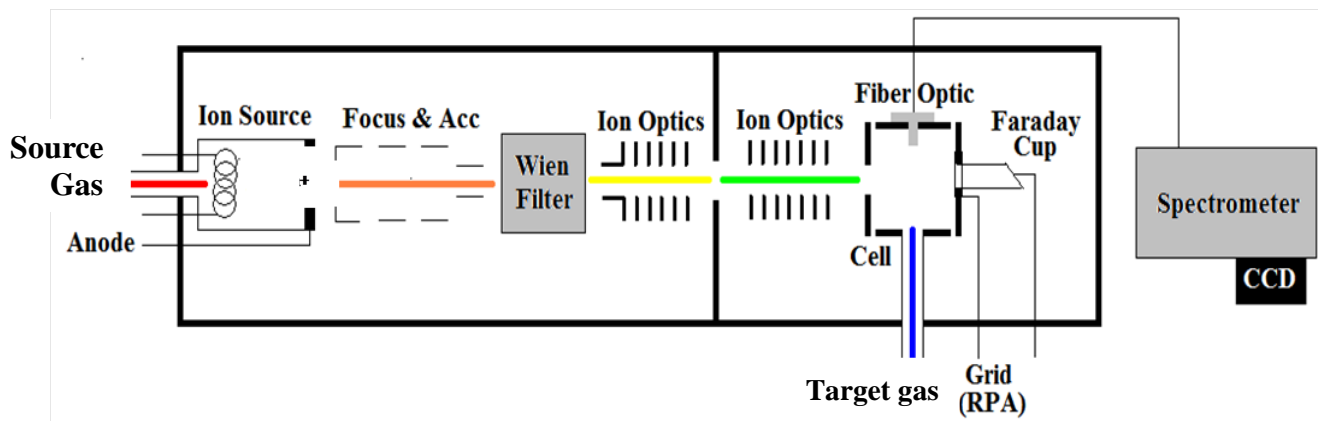
Figure 5: Schematic of the INCLUDE Apparatus

4. RESULTS AND DISCUSSION

4.1 Vacuum electrospray ionization study of the ionic liquid, [Emim][Im]

Ion emission from an externally wetted tungsten emitter supplied with the ionic liquid 1-ethyl-3-methylimidazolium bis(trifluoromethylsulfonyl)imide ([Emim][Im]) was studied at various temperatures. The emitter had a tip with approximate curvature of 20 µm. The electrospray plume angle, mass flow rate, total emission current, emitted species identification,

8

and species kinetic energy was explored for both cation and anion emission. In addition, thermochemical analysis was performed to predict the binding energy of selected ion clusters. The experimental apparatus used to perform this investigation was discussed in section 3.1. A brief accounting of the important findings will be discussed below. Full details of the methods, results, and discussion can be found in the associated journal publication.[1]
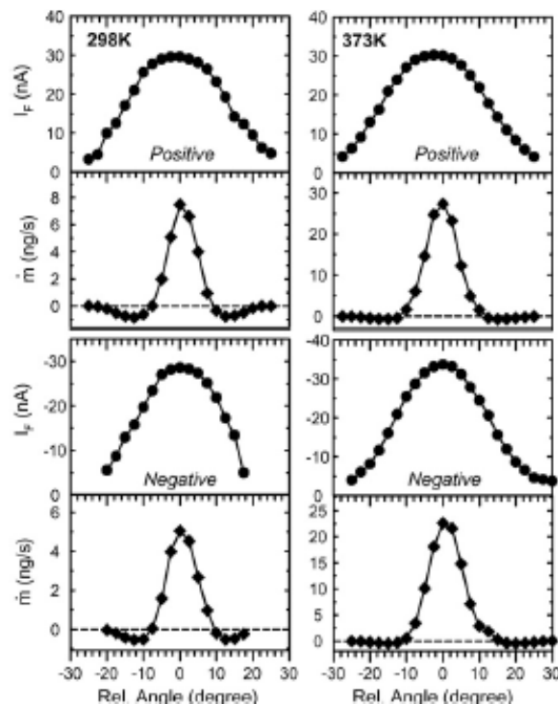
Figure 6: Near-field Sensor Measurements

The angular dependence of the emitted plume as measured by the near-field sensors for both polarities at two temperatures is shown in Figure 6. The emitted current, as shown in the I_F traces, is nearly constant at both temperatures for both polarities and appears largest along the centerline of the instrument, defined here as 0 degrees. The mass flow ($\dot{m}$) in all cases shows a significant positive mass flow down the centerline and negative values near +/- 10-15 degrees and trends toward zero at the edges of the plume. In contrast to the similarity of the emitted current at both temperatures, the mass flow is significantly more positive at the higher temperature for both polarities. This indicates that larger mass-to-charge values are expected at the higher temperatures. The comparison between $\dot{m}$ and I_F indicates that there is significant current at large angles associated with negligible mass flow.

At both temperatures and both polarities, it can be seen the QCM indicates negative mass flow near the wings of the distribution. Since the negative mass flow is at an angle where ion currents appear high, these negative contributions are attributed to the sputtering of deposited material from the QCM by high kinetic energy ions. In this experiment, the emitter needle is biased at approximately 500 V meaning that ions emitted without losses can expect to have kinetic energies near 500 eV per charge. These 500 eV ions collide with the QCM sensor crystal with significant velocity and remove material previously coated onto the sensor. As will be shown in later sections, heavier masses and those ions operating at lower kinetic energies (velocities) do not result in sputtering from the crystal.

Table 1: Cone-jet Parameters Determined for [Emim][Im] Wetted on a Tungsten Emitter

T (K)	300	300	373	373
K (S/m)	0.88	0.88	3.5	3.5
V_{ex} (V)	-1050	1050	-925	925
Polarity	+	-	+	-
I_o (nA)	65.4	54.2	114	108
I_F (nA)	29.6	28.6	30	34
$\dot{m}$(QCM) (ng s^{-1})	7.5	5.0	27.3	22.6
m/q (Daltons)	24,200	16,900	86,700	64,200
E_{max} (V/nm)	1.0	1.1	1.05	1.1
R_{max} (nm)	3.7	3.3	3.6	3.4

K is the temperature dependent conductivity; V_{ex} is the extraction voltage; I_o and I_F correspond to the total emission and Faraday cup currents, respectively; $\dot{m}$(QCM) is the mass flow measured on the QCM; E_{max} and R_{max} correspond to the maximum electric field strength and the associated radius of curvature at the jet neck (see journal publication)

Table 1 lists the parameters derived from the near-field targets, the FC and QCM, for the tungsten emitter at 300 K and at 373 K and separated according to the polarity of operation. The extraction voltage, V_{ex} is the voltage difference between the emitter and extractor. The I_o value is determined from a direct measurement of the current flowing from the emitter while I_F is the value of the FC over the centerline of the emitter (6 mm^2 area of acceptance). $\dot{m}$(QCM) is the mass flow measured down the center of the emitter with the same area of acceptance as the FC. m/q is the expected mass-to-charge ratio down the center axis as calculated from the I_F and $\dot{m}$(QCM) values. E_{max} and R_{max} are the electric field magnitude and radius of curvature of the jet neck calculated according to equations previously determined in the literature.[16] As the temperature is increased, the electrical conductivity and viscosity of the ionic liquid increases and decreases, respectively; this is reflected in the decreasing of the extraction voltage required to generate emission and the increasing of the total emitted current and mass flow from the emitter. The increasing gap between the current measured down the center to the total emission current as temperature is increased indicates the plume becomes more divergent at this higher temperature relative to the room temperature case.

The identity of small mass ions (<1200 m/q) could be determined by examining the plume using quadrupole mass spectrometry. Figure 7 depicts the mass spectrum of the plume for both cation and anion at 0 degrees and 20 degrees and for both temperatures. Species observed in the plume are the [Emim]$^+$ cation at 111 m/q, [Emim]$^+$([Emim][Im]) at 502 m/q, and [Emim]$^+$([Emim][Im])$_2$ at 893 m/q for the positive polarity and [Im]$^-$ at 280 m/q, [Im]$^-$([Emim][Im]) at 670 m/q, and [Im]$^-$([Emim][Im])$_2$ at 1062 m/q for the negative polarity emission. We have often referred to these species as the n = 0, 1, and 2 species, respectively, where the n value indicates the number of neutral pairs solvating the cation or anion. This terminology will be used throughout the remainder of the report.

The results presented in Figure 7 are all normalized to the same intensity value. In all of the on-axis mass spectra taken, the baseline is seen to offset from zero indicating that some species are not completely being removed from the quadrupole at these angles. Based on the increased mass flow down the center axis and the expectation that ions with m/q values > 10000 amu/q exist, the offset baseline indicates these species are not being filtered efficiently by the quadrupole and are contributing to a constant background. The off-axis spectra also have

significantly more intense ion contributions as measured by the intensity of the peaks, again in agreement with the findings of the near-field measurements. Finally, increasing the temperature does not appear to alter the species observed with the quadrupole although a small increase in the n = 2 population is observed and the droplets associated with the baseline appear to increase for the on-axis spectra, as expected for the increased mass flow at higher temperature.
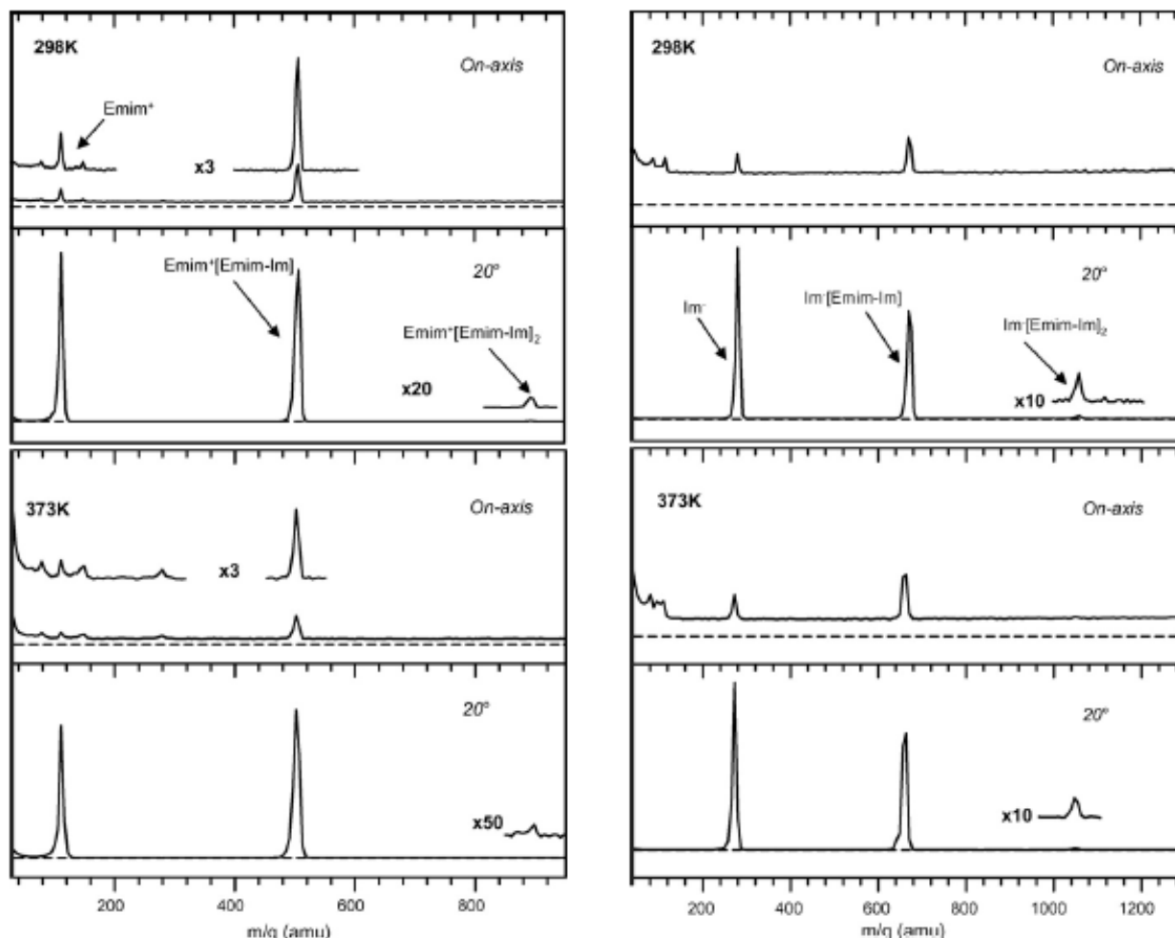
Figure 7: Mass Spectra of the Plume of [Emim][Im] Emitted from a Tungsten Emitter
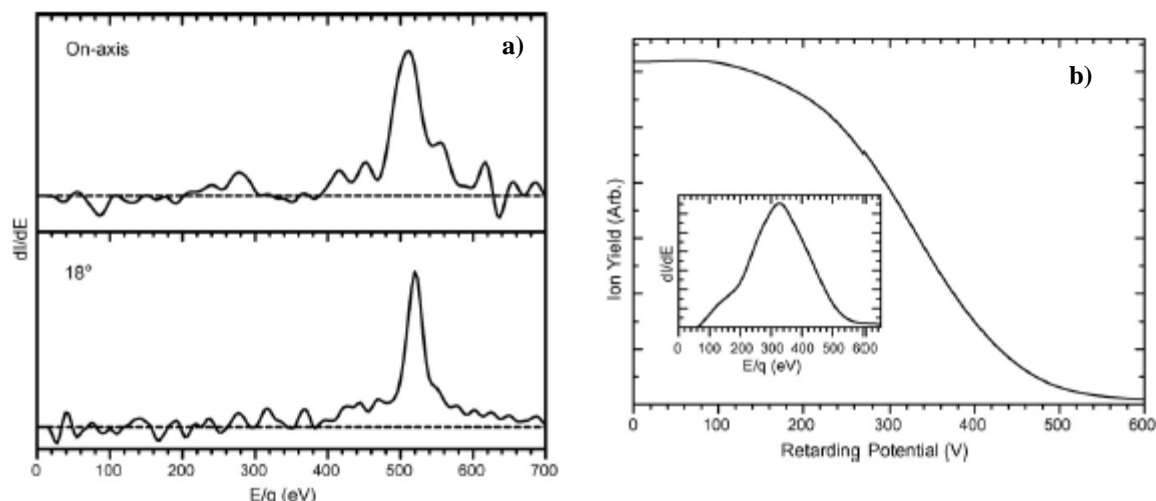
Figure 8: RPA Analysis of [Emim][Im] Emitted from a Tungsten Emitter

Figure 8 shows the room temperature retarding potential curve for $[Emim]^+$ produced on-axis and off-axis in a) and the high m/q species (>1200 m/q) that make up the baseline in b). The results of $[Emim]^+$ are essentially identical those for the n = 1 cluster (not shown). The RPA of the $[Emim]^+$ indicates the bulk of these emitted cations have kinetic energies very near the emitter bias potential (+500 V) and are emitted without loss from the neck of the Taylor cone. The kinetic energy of the large masses appear centered near 300 eV with a very wide energy distribution indicating their origin is not the same as that of the smaller ions. Loss of kinetic energy relative to the emitter bias is expected if a jet structure protrudes from the Taylor cone and extends away thus reducing the potential the liquid experiences. In this work, it was postulated that the RPA can be used as an analytic technique to determine the emission origin of a particular species based on its kinetic energy relative to the emitter potential. If a species is formed in the early cone-jet region (called the neck), it is expected that it will have a population distribution centered off-axis and have a kinetic energy near that of the emitter potential. If a species is emitted downstream into the transition region or the jet, it is expected these ions will suffer ohmic losses and have kinetic energies below that of the emitter potential. In addition, the population distribution of these species will be more generally peaked about the center axis.

In this investigation and the many others explored in this research task, electrochemistry between the ionic liquid and the emitter surface proved to be an important experimental consideration. Figure 9 depicts the current measured on the FC and the associated positive polarity mass spectrum while operating in a single polarity for an extended period of time. When switched from AC to DC operation, the I_F current measured on the FC rapidly decayed to just a few nA over the first 100 minutes where it persisted out to >4000 min. The value returned to normal operation nearly instantly once returned to the AC operational mode. The associated mass spectra down the center axis at each time value were also recorded. The appearance of new ions and the disappearance of the baseline associated with the droplets were observed. The new ion species could be assigned to the clusters involving the neutralization of the anion, i.e. $Emim^+-Im^0$. These newly formed ions also disappear rapidly once AC operation is restored.

12
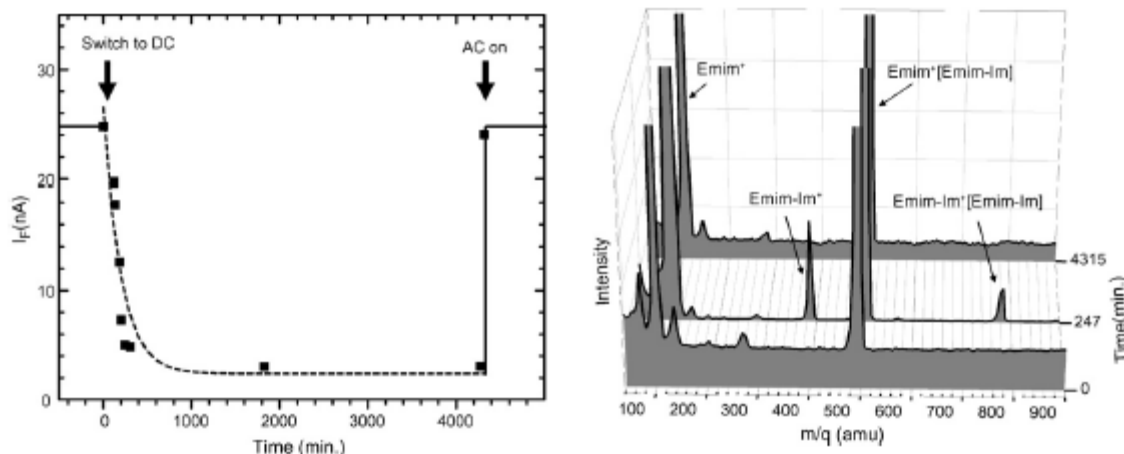
Figure 9: Current and Mass Spectrum of [Emim][Im] Operated in Positive DC Polarity

The mechanism behind the disappearance of the current and the appearance of the new species and the nearly instantaneous recovery in AC mode is now further elaborated. The observations suggest that electrochemical transformation of the emitter-ionic liquid interfacial properties are throttling the flow of the ionic liquid across the emitter surface, in essence, reducing the ionic liquid flow rate. One method for the throttling to occur is through the formation of an electrochemical double layer, where a surplus of negative charge forms at the liquid-metal interface while operating in the positive polarity. Once the layer is formed, a layer of positive polarity forms above the negative layer immobilizing those cations. Continued build-up of the alternating charged layers would ultimately lead to a reduction in the flow of liquid, as the flow rate would be hindered by the strong attraction of the liquid film to the now-immobilized double layer of ionic liquid. Once the polarity is reversed, rapid disintegration of the original double layer is expected and formation of a double layer of opposite polarity begins anew.

4.2   Nanojets, Electrospray, and Ion Field Evaporation

Molecular Dynamics simulations combined with experimental measurements of a charged liquid composed of sodium iodide (NaI) dissolved in formamide at select ratios or potassium iodide (KI) dissolved in formamide at select ratios was investigated to attempt to improve the understanding of the microscopic physics occurring at the emitter interface . In the experimental investigations, these solutions were electrosprayed using a capillary emitter of tip diameter equal to 5 µm and with the experimental apparatus described in section 3.1. The theoretical methodology is rather extensive and interested readers should consult the full publication report for all of the specific details.[2] The bulk of the theoretical approach relied on molecular dynamics methods to determine the effects of external electric fields on charged droplets of a certain radius of the charged liquid of interest. In this section, the key experimental results will be presented first followed by the key findings of the theoretical investigations. Similarly to the ionic liquid results presented in section 4.1, the "n" notation will be used to indicate the number of formamide molecules attached to a parent cation or anion (solvation number).
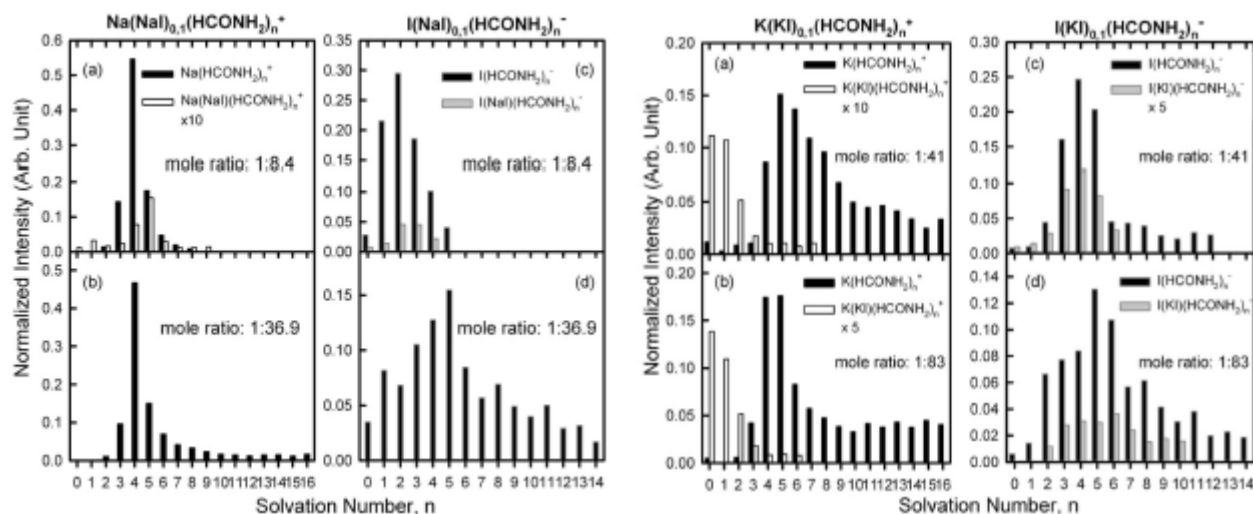
Figure 10: Solvation Number Distributions for Electrosprayed Salt-Formamide Solutions

Figure 10 presents the solvation number distributions for both the NaI and KI dissolved in formamide solutions for two different concentrations per liquid. In the NaI-formamide solution, the observed solvation number broadens as the solution becomes less concentrated (1:36.9) although the most probable cation does not change (~n = 2). The anion also broadens but a greater shift in the most probable anion occurs. The more complex ions $[Na^+(NaI)(HCONH_2)_n]$ are only present in the more concentrated solution for both the cation and anion species. In the KI-formamide solutions, similar to the cation spectrum of the NaI-formamide, dilution of the solution only results in a small shift in solvation numbers. However, the distributions extend to significantly higher solvation numbers compared to the Na^+-based results. The complex ions are generally more abundant than the NaI solutions and also appear to be present in the dilute KI solution.

The thermochemistry of sodium-formamide cations and potassium-formamide cations, was investigated using density functional theory with the B3LYP functional and a 6-31G(d) basis for the cations. Iodide-formamide anions were calculated with Moller-Plesset second-order perturbation theory (MP2) and the 6-311+G(df) basis set for iodine. In both cases valid minimum energy structures were located and stationary points verified through a positive definite Hessian analysis. The zero-point energy (E_{ZPE}), the internal energy (E_{int}), and single solvent molecule dissociation energy ($D(MF_{n-1}-F)$) is presented in Table 2 for these clusters. The internal energy is defined as the energy above the zero-point energy resulting from calculation at temperatures above 0 K and is calculated for 298.15 K. The dissociation energy is the energy required to remove one formamide solvent molecule from the parent cation or anion. All energies are in kcal/mol. It is seen in Table 2 that the internal energy at 298.15 K exceeds the binding energy for ions with a solvation number above n = 4 for the cationic solvated ions (Na^+ and K^+), and above n = 3 for the I^- solvated ions, respectively. These results predict that solvated ions above these n solvation numbers are thermally unstable and, given sufficient time, will dissociate by desorbing a formamide molecule.

Table 2: Thermochemistry of Solvated Ion-Formamide Clusters

	$Na^+(HCONH_2)_n$			$K^+(HCONH_2)_n$			$I^-(HCONH_2)_n$		
n	E_{ZPE}	E_{int}	$D(MF_{n-1}\text{-}F)$	E_{ZPE}	E_{int}	$D(MF_{n-1}\text{-}F)$	E_{ZPE}	E_{int}	$D(MF_{n-1}\text{-}F)$
1	30.1	3.33	39.7	29.8	3.46	28.7	27.8	3.6	17.4
2	59.9	6.71	33.3	59.3	7.02	24.0	56.0	7.0	14.9
3	89.4	10.3	24.1	88.7	10.6	19.5	83.7	10.8	12.1
4	118.4	14.0	17.2	117.7	14.4	15.6	111.8	14.3	10.9
5	149.5	16.3	15.7	148.8	16.8	14.4	140.0	17.1	8.4
6	178.2	20.2	7.2	178.3	20.3	10.8			

A comparison of the predicted stable species against the experimental data presents a number of problems. The experimental data indicates clusters significantly larger than the thermochemistry limit exists. One possible hypothesis is that the experimentally emitted ions complete traversal of the experimental apparatus in roughly 25 µs, and have simply not had enough time to evaporate. Another hypothesis is that the observed ions are significantly colder than 298.15 K, likely through evaporation of formamide ions from larger n clusters resulting in significantly colder temperatures. This approach is often termed *evaporative cooling*.

Since the experimental flight time could not be altered owing to the fixed nature of the experimental apparatus, the first hypothesis was examined through calculation of an ion survival fraction through theoretical means best described in detail in the full publication. The output of this calculation compared the survival fraction at t = ∞ to that at t = 26, 28, and 31 µs, typical of the flight time of the n = 4, 5, and 6 cations through the apparatus, respectively. At 300 K, the survival fraction at t = ∞ was approximately 93%, 75% and 80% of the value at the apparatus timescales. At T = 400 K, these values changed to 46% and 50% for the n = 4 and 5 ions, respectively. These results indicate that some thermodynamically unstable molecules likely survive as metastables by the time they collide with the detector, skewing the results towards higher solvation number.

Simulations of a 10 nm NaI-formamide droplet at an approximate 1:8 ratio were explored using molecular dynamics with various applied electric field strengths. A spherical droplet of approximately 7150 formamide molecules and 900 NaI units was generated, corresponding to a similar concentration to that of the concentrated NaI-formamide solution experimentally investigated. In the presence of a uniform electric field of at least 0.625 V/nm, the original sphere is observed to elongate along the electric field axis. As the aspect ratio continues to increase, at around a value of 5 to 6, a jet is observed to form at the ends of the mass. Emission of droplets and ions then occurs and several observations are discussed below.

Figure 11 depicts several properties of ions emitted from the 10 nm droplet and detected 200 nm downstream in both directions. In these simulations, cations and anions fly in opposite directions due to the directionality of the external electric field. On the left side of Figure 11, the effective electric field (in V/nm) on the surface of the cluster, the q/m ratio of the cluster and the $q/q_{Rayleigh}$ value is calculated as a function of the emitted cluster radius. The surface electric field is calculated from Coulomb's law and levels off at approximately the experimental value as R increases. Similarly, the |q|/m and q/q_{Ray} ratios follow a trend expected from previously determined equations. Essentially all clusters observed in the simulation have radii smaller than R_{max} determined from the experimental measurement. The two right panels of Figure 11 depict the fraction of ions determined from the simulations at two different electric fields, 1.0 V/nm and 1.5 V/nm. The most significant emission at both external electric field strengths occurs from

species with a single net charge with decreasing significance of clusters with higher charge values. Finally, for those single charged clusters, the most probable resulting ion is the $n = 0$ cation or anion with a decreasing fraction of $n = 1$ and $n = 2$ species.
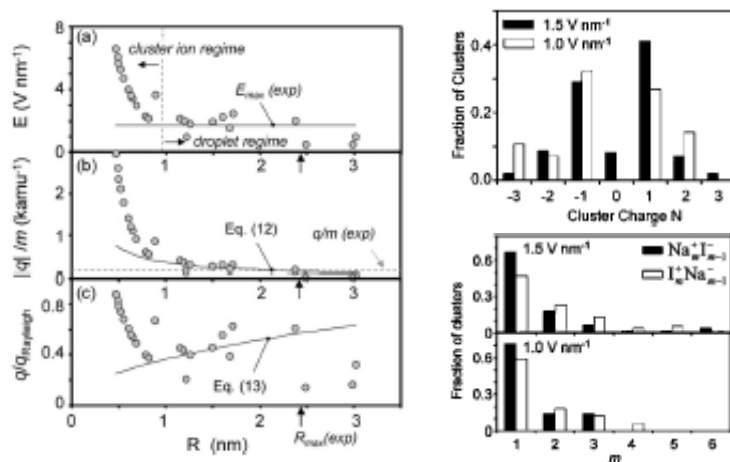
Figure 11: MD Simulation Results of 1:8 NaI-Formamide Droplet

4.3   Electrospray Plume of [Emim][Im] on a Tungsten Ribbon Emitter

Droplet emission depending on the flow rate of the IL was presented and discussed in section 4.1. In this section, attempts to modulate the flow rate of the ionic liquid by making use of a ribbon as opposed to needle type emitter and probing the resulting plume for differences are made. The ribbon was fabricated from electrochemical etching to a 750 µm wide/50 µm thick ribbon with tip width of ~20 µm and ~1 µm thickness. Near-field and mass spectrometric measurements are made using the apparatus described in section 3.1. This section will summarize the important findings of the experiment and the interested reader is encouraged to read the full published document for complete discussion of the experiment, results, and conclusions.[3] The choice of emitter is unusual compared to other sections in this report and is described in some detail. Figure 12 depicts the lab orientation of the ribbon emitter, which is broken into two orientations: vertical and horizontal. The center line of the experimental apparatus is taken as the z-axis. The thruster rotation is always in the xz plane. The horizontal orientation has the width of the ribbon in the xz plane, parallel with the plane of rotation. The vertical orientation has the width of the ribbon in the yz plane, perpendicular to the plane of rotation.
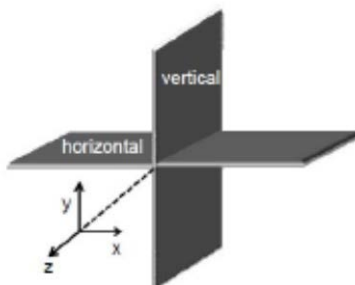
Figure 12: Ribbon Orientation Definition
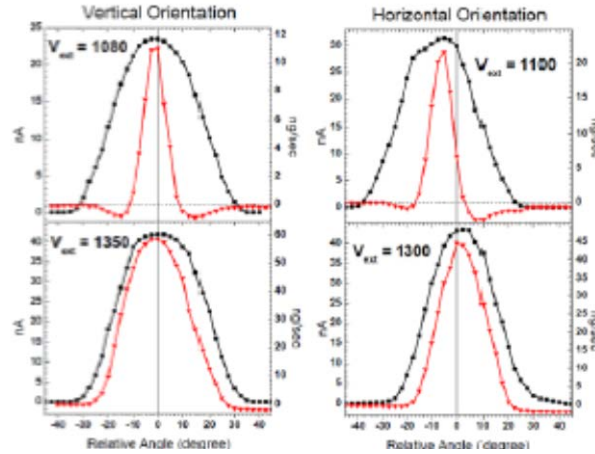
Figure 13: Near-field Results for [Emim][Im] on a Ribbon Emitter

The angular dependence of ion current and mass flow as measured by the FC and the QCM for positive polarity is presented in Figure 13 for both orientations and at two different extraction voltages. The black squares are the current measurements whose values are portrayed on the left axis in units of nA while the red triangles are the mass flow measurements and are represented along the right axis in ng/s. At low extraction voltages, measurable amounts of current extend to relatively high spray angles approximately 30 degrees on either side of thruster center. The mass flow measurements indicate a narrower distribution and have evidence of the sputtering behavior previously presented in Section 4.1. Figure 13 also shows near field measurements taken at higher extraction voltages for both orientations. Compared to the lower extraction voltages, the total amplitudes of both the Faraday cup and the QCM readings are somewhat higher. In particular, the mass flow and current profiles appear to be nearly equally wide.

A summary of the near-field measurements for the two ribbon orientations, polarities, and extraction voltages is presented in Table 3. The voltage required to induce emission from the ribbon emitter was found to be ~1100 V in both orientations. The ratio of I_F to I_o gives some idea of the degree of plume divergence and was demonstrated for the cations in Figure 13. A large average m/q value is observed for all emitter conditions, indicative of droplet formation, with no evidence of ion-only emission. Increasing the extraction voltage by approximately 25% generally doubled the total emission current, quintupled the mass flow and generated significantly larger average m/q values.

Table 3: Near-field Electrospray Parameters for [Emim][Im] on a Ribbon Emitter

Orientation	Vertical				Horizontal			
Polarity	+	-	+	-	+	-	+	-
V_{ext}	1080	1150	1350	1400	1100	1070	1300	1300
I_o	170	176	324	302	186	183	324	328
I_F	23.5	26.7	42.3	50.9	31.3	21.0	44.3	43.9
$\dot{m}$(QCM)	11.0	13.7	58.4	54.0	21.6	12.0	88.0	91.6
m/q (amu)	45,000	49,000	133,000	102,000	67,000	55,000	191,000	201,000

17
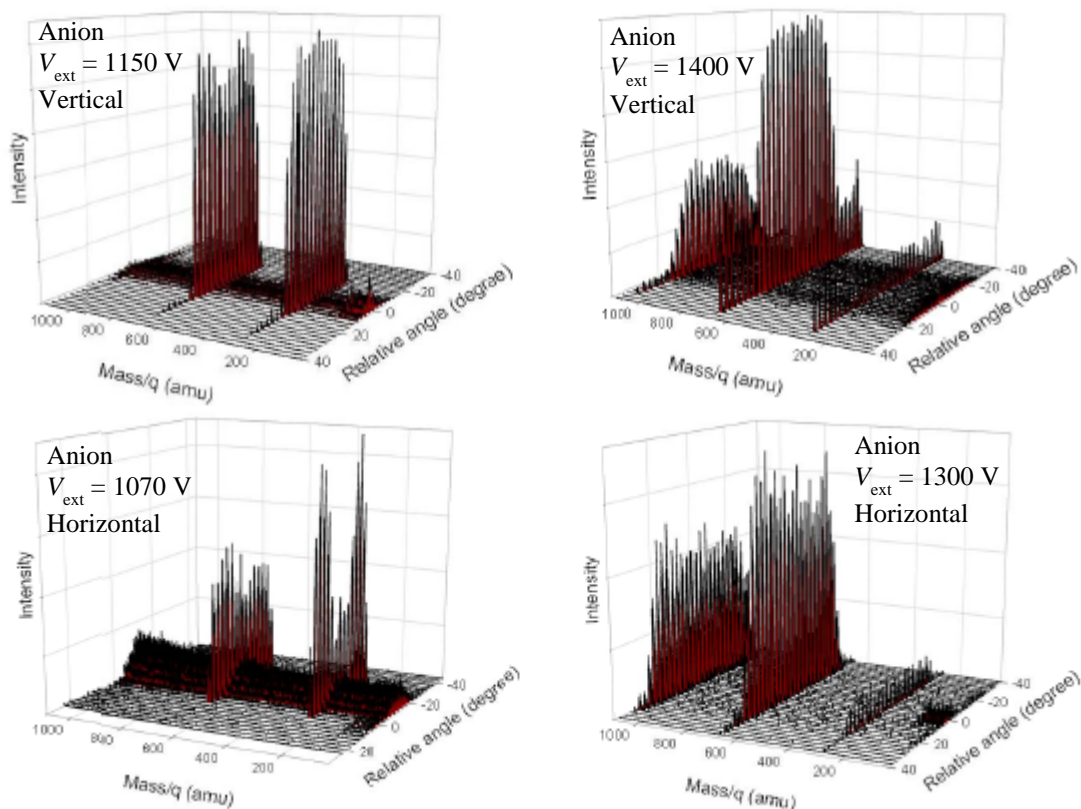
Figure 14: Anion Mass Spectra of [Emim][Im] on a Ribbon Emitter

Figure 14 shows the anion mass spectra obtained as a function of thruster angle from the vertical and horizontal orientation of the ribbon at low and high extraction voltages. The two dominant peaks in the mass spectra correspond to the [Im]⁻ anion at 280 amu/q and [Im]⁻ ([Emim][Im]) at 671 amu. The [Im]⁻([Emim][Im])₂ anion is observed with much less intensity at the low extraction voltage but considerably larger relative intensity at the higher extraction voltage. The ion signal shows an angular spread of about +/- 20 degrees for the vertical orientation with the intensity roughly equal in this region. The n = 0 ions at 280 amu/q in the horizontal orientation exhibit the pattern expected for neck type emission with the ion distribution maximized off-center. In contrast, the high extraction voltage in the horizontal orientation highlights the wide spray of emitted species covering nearly +/- 40 degrees from the center with nearly uniform intensity distributions at all angles. In addition, the intensity of the n = 0 anions has nearly vanished and has been replaced with larger portions of n = 1 and n = 2. The background detected throughout the mass spectrum at small angles is attributed to droplets with high m/q that are not rejected by the quadrupole mass spectrometer. The apparent less population of droplets it in the higher V_{ext} cases is explained by the fact that the quadrupole mass filter and detection system are actually more sensitive to smaller m/q values closer to the upper mass limit of the quadrupole. Because the average m/q value of the droplets, as judged from the near-field measurements, increases significantly with extraction voltage, the large droplets are simply rejected more efficiently than those with m/q around 30,000 amu/q.

Using a ribbon emitter and allowing alteration of the extraction voltage was an attempt to alter the liquid flow rate in a controlled fashion. The results presented above indicate that at the lowest extraction voltage, the ribbon may approach the flow rate of a typical needle and its

respective mixed ion-droplet operating regime. Energy analysis of the detected ions (not shown) for low and high extraction voltage indicate that at 30 degrees off-axis, the n = 1 cation has an energy distribution centered at the bias potential of 500 V for the low extraction voltage but shifts to 400 V for the same ion at the higher extraction voltage. Those ions detected down the center axis exhibit two different energy distributions with distinct peaks at 520 V and 400 V suggesting the emission mode at high extraction voltage may consist of emission from two distinct regions on the emitter.

4.4 Aspect Ratio Dependence of the Electrospray of [Emim][Im]

Now having firmly established the importance of the liquid flow rate on the emitted species through the fabrication of a ribbon emitter with different dimensions in both orientations, an attempt to fabricate a pair of emitters with different aspect ratios using controlled means was undertaken. In this section, a pair of needle-like emitters was fabricated with different aspect ratios, notably a 1 mm base with a 2 mm and 3 mm length, respectively, using porous tungsten. A photograph and schematic depiction of the aspect ratio of the emitters used in the study is presented in Figure 15. Similar to the previous ionic liquid investigations, the ionic liquid [Emim][Im] was the liquid employed in the study and the experimental apparatus described in section 3.1 was used for the experimental work. This results in this section appear in a conference proceeding covering the same topic area and interested readers are encouraged to consult the publication for full detailing of the experimental methods, results and conclusions.[4] The important results and findings will be presented below.
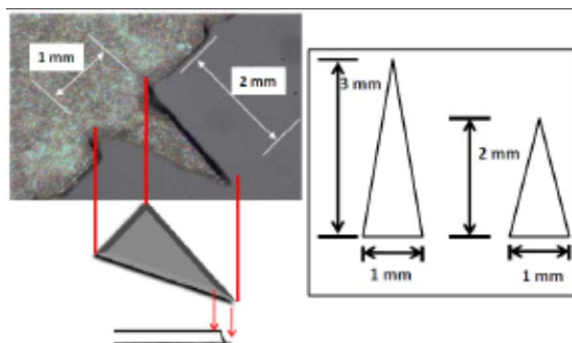
Figure 15: Aspect Ratio Comparison of the Porous Tungsten Emitters

Figure 16 shows the AC mode FC and QCM measurements taken as a function of thruster angle for both the 3 mm and 2 mm aspect ratio emitters. The black squares represent the emitted current measured on the FC during the positive polarity component while the black triangles detail the emitted current measured during the negative polarity component for both emitters. The mass flow is denoted by red circles and represents the time-averaged combination of both polarities. In both cases, the plume, as judged by the current measurements, extends approximately +/- zero degrees with similar measured current values in both cases and appears largely symmetric about 0 degrees. The mass flow is significantly larger for the 2 mm emitter as compared to the 3 mm emitter maximizing at about 40 ng/s down the center axis as compared to 6 ng/s for the 3 mm emitter. The 3 mm emitter also exhibits negative going mass flow near +/- 10 degrees before leveling off at near 0 values at high angles. The total emission current for the 2

and 3 mm emitter was 200 nA and 150 nA, respectively. The center axis average *m/q* values are approximately 117,000 and 23,000 amu/q for the 2 and 3 mm emitter, respectively.
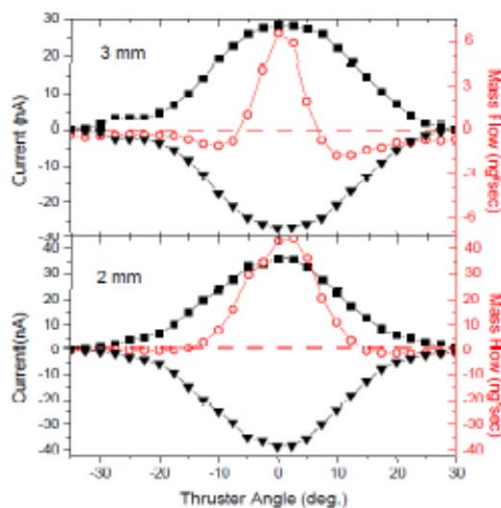
Figure 16: Near-field Comparison of the Emitter Aspect Ratio Study of [Emim][Im]

The angular dependence of the cation and anion mass spectra is plotted in Figure 17 for both the 2 and 3 mm emitter. Beginning with the cation spectra and in the case of the 2 mm emitter, the detected angle is fairly wide, mirroring the near-field FC measurement and appears relatively flat across the top although some evidence of a slight peaking at +/- 10 degrees is evident. The 3 mm has roughly the same plume expanse but is clearly peaked at +/- 10 degrees and shows no evidence of the n = 2 cation at 893 amu as observed in the 2 mm emitter case. The 3 mm case shows evidence of significant droplet contribution while the baseline is small along the center axis for the 2 mm case. This behavior was exhibited in the ribbon results as well, where it was noted that when the *m/q* value of the droplets greatly exceeds the upper range of the quadrupole it is less likely to be detected. Similar behavior is observed in the anion spectra for the same emitters, the 3 mm exhibits a baseline signal along the center axis and ions peaked off-center at approximately 10-15 degrees with only the smallest amount of n = 2 cations present. The 2 mm emitter exhibits a small amount of baseline but has significantly more n = 1 and n = 2 than the 3 mm emitter. In addition, the anions appear centered similarly to the cation case.

The combined mass spectrometer data and near-field measurements indicate that the 3 mm emitter exhibits a lower flow rate than the 2 mm emitter although not low enough to reach pure ion emission. Both emitters appear to operate in a mixed ion-droplet mode although the droplets generated down the center axis in the 3 mm have significantly smaller m/q values than those originating from the 2 mm emitter, indicating that the longer aspect ratio has decreased the liquid flow rate by some degree. In addition, the mass flow data of the 3 mm emitter exhibited negative mass flow at the +/- 10 degrees indicating that the beam emitted at these angles is dominated by small mass ions moving with high kinetic energies capable of sputtering material off of the QCM.
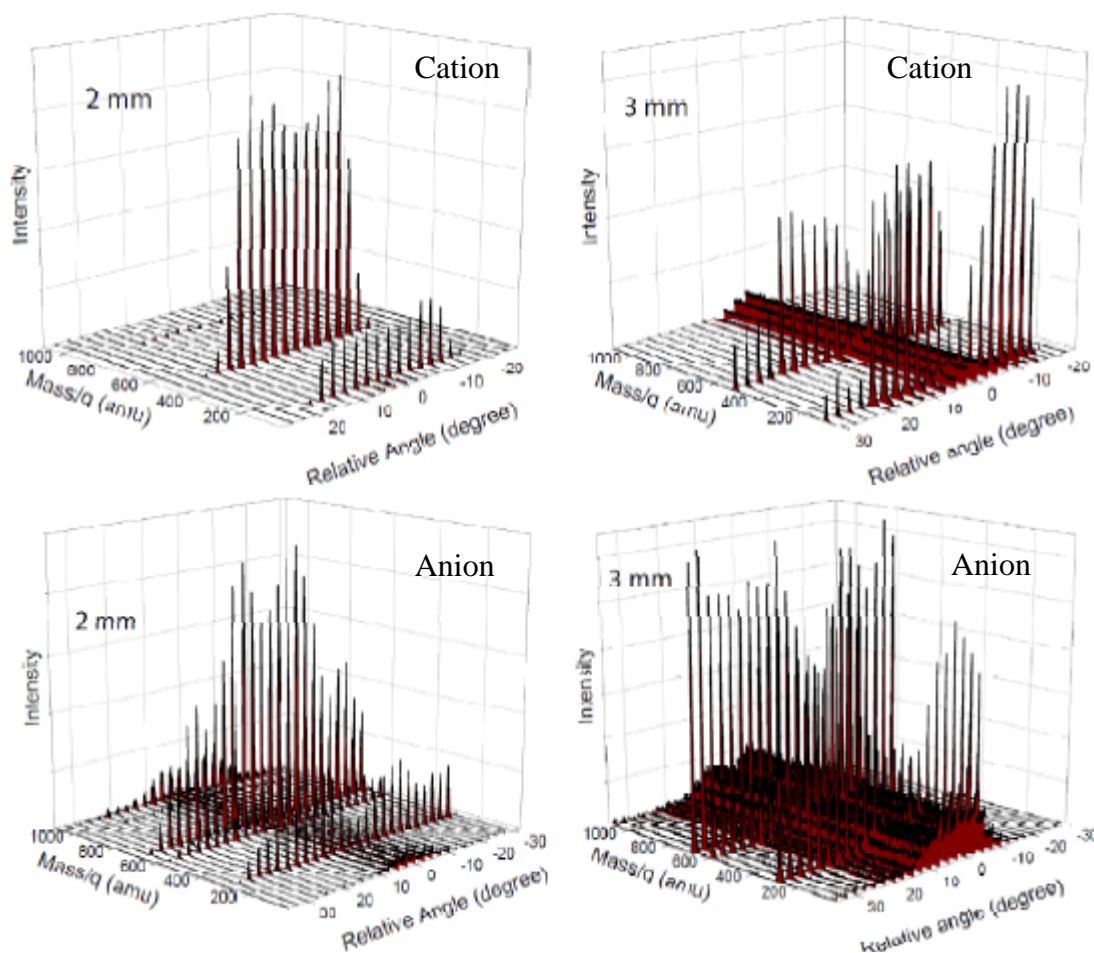
Figure 17: Mass Spectra of [Emim][Im] from Various Aspect Ratio Emitters

4.5 Variable Flow Rate Operation of [Bmim][DCA]

Direct investigation of the ionic liquid flow rate is possible through the use of a capillary emitter with active backing pressure control. In this section, the ionic liquid 1-butyl-3-methylimidazolium dicyanamide ([Bmim][DCA]) is investigated using a 50 µm capillary tip. The experimental apparatus used to generate the results in this section is discussed in section 3.1 with the capillary fluid flow system described in Figure 3. The FC and QCM were modified with smaller apertures to allow angular resolution of 2.5 degrees for the plume. The key findings and discussion will be included in this section while the interested reader should consult the full length journal article for a complete description of all the findings, methods, and details in this experiment.[5] The added dimensionality of controlling the IL flow rate necessitated an experimental simplification, notably, that this investigation only examined the positive polarity emission. As such, only cation mass spectra were explored.

The flow system was first calibrated over the backing pressure range of 50 to 230 torr encompassing flow rates of 0.3 to 2.18 nL/s of the ionic liquid. This was calculated using two methods: introduction of bubbles and direct measurement of their movement and through complete plume measurement of the mass flow as measured by the QCM at low liquid flow

rates. The linearity of pressure to volumetric flow rate was confirmed and reproduced multiple times with the extraction voltage on and off.
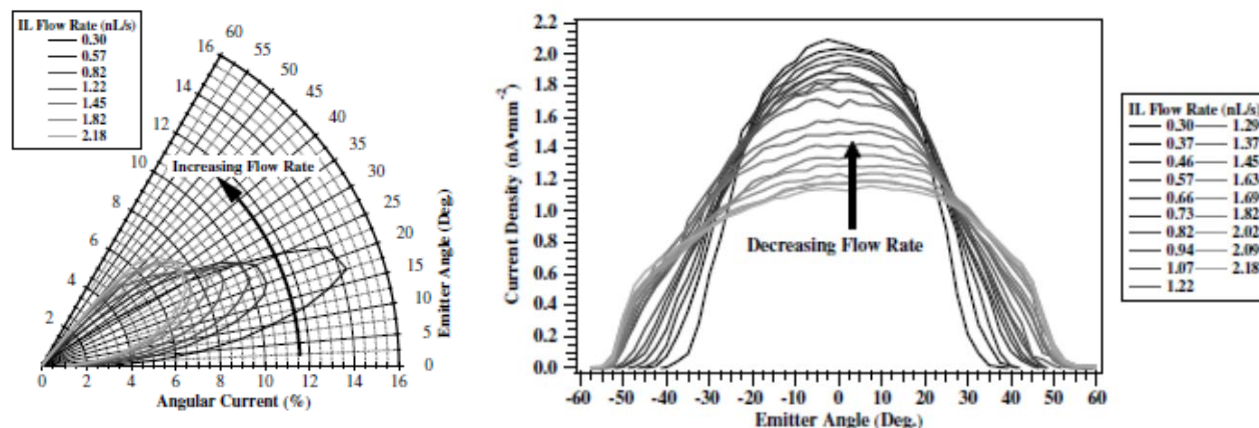
Figure 18: Flow Rate/Angular Dependence of the Current Density

The angular dependence of the current density as a function of volumetric flow rate is depicted in Figure 18. The expanse of the plume is narrowest at the lowest flow rate encompassing +/- 30 degrees slightly larger than the plume expanse observed with needle emitters. The current density reaches its most significant value down the center axis at the lowest IL flow rate. As the IL flow rate increases, the plume broadens significantly and simultaneously decreases down the center axis relative to the lowest flow rate sampled. At high flow rates, evidence of the ion beam impinging on the extractor is apparent as determined from current measurements made on the extractor. An alternate way to view the effect of flow rate is through a polar plot where the % of current at an angle is depicted for the entire plume. At the lowest flow rate, 14% of the total current is located between 15-20 degrees while only 5% of the total current occurs in the same range at 2.18 nL/s. Clear shifting of the angular current percentage maximum from 17.5 degrees to 27.5 degrees is easily seen in the polar plot with increasing flow rate.

A complete accounting of current emitted from the capillary is shown in Figure 19. The emitter current is measured through a resistor circuit and reflects the I_o values presented in previous sections. A similar monitoring circuit was established on the extractor to account for the increased current that strikes the extractor at higher flow rates. The integrated beam current is determined from the near-field measurement on the FC over the entire emitted plume and is akin to the I_F values described previously. Since collision of the ion beam with the extractor was evident, a combined I_F plus the current striking the extractor, I_{ext}, was also calculated. Finally, a curve fit employing a power law was used to fit the current measured directly off the extractor. This combined FC current plus the extractor current neatly mimicked the emitter current indicating that the analysis using the FC effectively samples the entire plume. The amount of current striking the extractor rises from 0 nA at the lowest flow rates to constituting roughly 50% of the total current at the highest flow rates reflecting the significant increase in plume divergence as a function of flow rate. The power law fit to the current profile agreed well with empirical current (I) scaling laws presented in previous investigations of electrospray systems adding more evidence of the efficacy of the near-field approach adopted in this experiment.
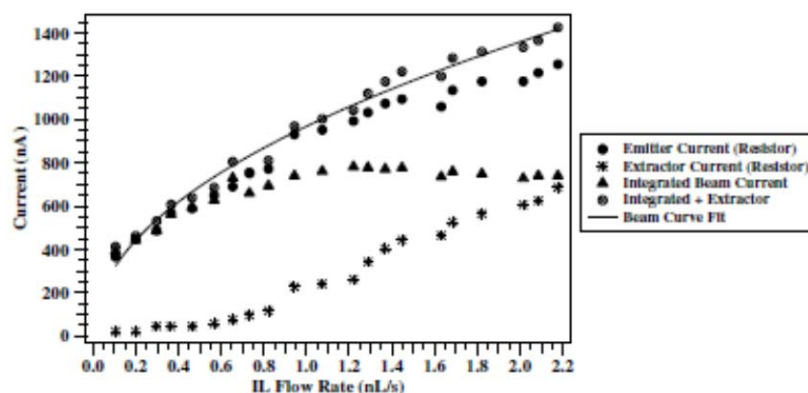
Figure 19: Emission Current as a Function of the IL Flow Rate

The angular dependence of the mass flow rate as a function of ionic liquid flow rate is presented in Figure 20. The mass flow rate trends indicate increasing mass flow rate values at the center of the plume and increased mass flow rate values at high angles. Only selected IL flow rates were sampled and only one side of the plume under the assumption that the plume would be symmetric about the center axis. Select flow rates were sampled because the QCM experienced unreliable results if extended periods of sampling at high flow rates occurred. This likely results from the complication that the IL, once pooled onto the QCM sensor crystal, was incapable of evaporating away over time and instead resulted in bubble formation on the crystal at high flow rates invalidating the thin film approximation. To counter this issue, we chose a limited number of flow rates and limited sampling of the highest mass flow rate positions. No evidence of sputtering of material off the crystal sensor was observed.
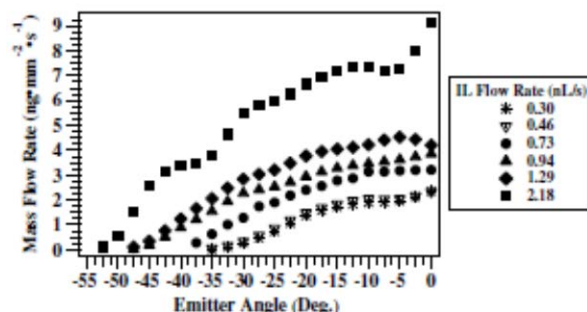
Figure 20: Mass Flow Rate Angular Dependence as Function of IL Flow Rate

The increased mass flow rate down the center axis as IL flow rate is increased coupled with the decrease of the emission current down the center axis suggests that the average m/q value significantly increases over the IL flow rate range sampled. The current, mass flow rate ($\dot{m}$), and mass-to-charge ratio (m/q) of selected IL flow rates is presented in Table 4. The integrated current is the I_F values described above. The emitter current is the I_o value as measured by the resistor circuit on the emitter. The current difference is the percent difference between I_o and I_F reflecting the divergence of the plume. The extractor current is measured using a resistor circuit attached to the extractor. The integrated $\dot{m}$ value is determined by integrating the QCM values and is only available at selected IL flow rates. The nominal mass flow rate is determined from the volumetric flow rate times the density of the ionic liquid. The integrated

m/q value is calculated from taking the integrated mass flow rate divided by the integrated current. The final column is the calculated *m/q* ratio assuming the nominal mass flow and the best fit to the emitter current profile.

Table 4: Summary of Near-field Measurements for [Bmim][DCA] at Select Flow Rates

Flow rate, nL/s	Integrated Current, nA	Emitter Current, nA	Current Difference, %	Extractor Current, nA	Integrated $\dot{m}$ ng/s	Nominal $\dot{m}$ ng/s	Integrated *m/q*, amu	I(beam) *m/q*, amu
0.30	486	487	0.2	45	454	317	90,000	95,000
0.46	594	589	0.8	45	503	493	82,000	117,000
0.73	660	751	12.1	95	885	779	129,000	148,000
0.82	694	772	10.1	116		874		157,000
0.94	740	931	20.5	227	1590	1003	207,000	168,000
1.29	778	1032	24.6	342	2046	1369	254,000	197,000
1.45	777	1094	29.0	443		1539		209,000
1.82	749	1176	36.3	565		1937		234,000
2.18	740	1255	41.0	686	4335	2315	566,000	256,000

The angular dependence of the mass spectra is presented in Figure 21 for three flow rates: a) 0.27 nL/s, b) 1.24 nL/s, and c) 2.18 nL/s. The lowest flow rate contains all of the possible cations that can be detected within the quadrupole mass range including the n = 0 to n = 4 cation species. The ion distribution is maximized at the n = 1 species with relative populations decreasing as n changes. Some evidence of a slightly off-center maximum appears to exist although not as clear cut as some of the previous investigations discussed in this report. The higher flow rate mass spectra are nearly devoid of the n = 1 cluster and instead populated more by the higher n species of n = 2 – 4. The mass spectra were taken with identical voltages applied to the channeltron and in reasonably quick succession which should allow relative quantification of the intensities of the various ions. As such, the small ion intensity is significantly less at larger flow rates consistent with the formation of an increasing number of droplets. At the 1.24 nL/s flow rate, the n = 2 cluster shows the most intensity but by 2.18 nL/s the n = 4 cluster is the most significant. This distribution alteration provides an additional and significant confirmation of the effect of liquid flow rate on the observed ion populations. The lack of baseline signal in the mass spectrum down the center axis indicates that the droplets are large *m/q* values consistent with the findings of the larger *m/q* droplets postulated in previous sections. Additionally, the distribution of ions appears symmetric about the center axis at the higher flow rates with no evidence of peaking at -10 degrees.
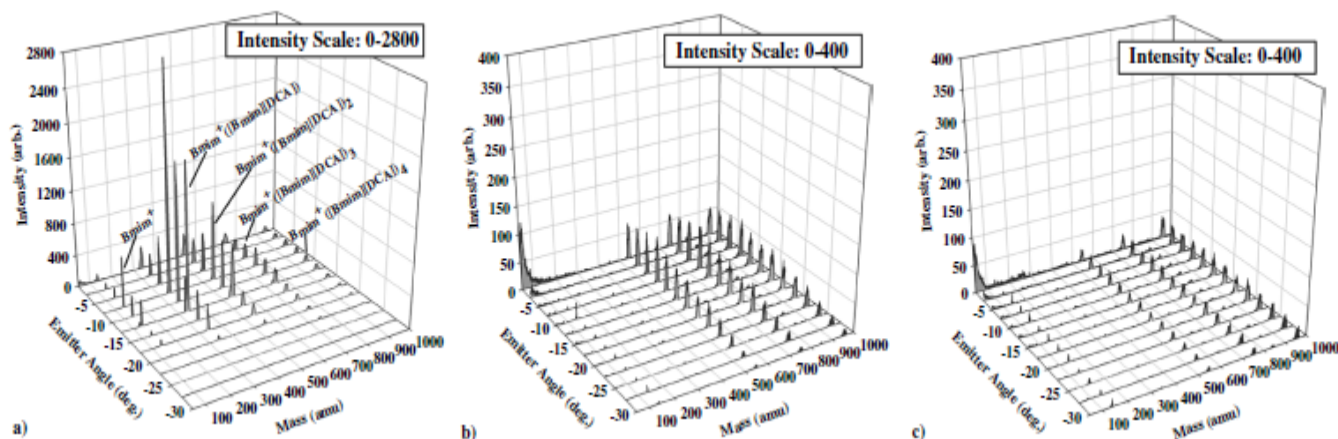
Figure 21: Angle-resolved Cation Mass Spectra at Select [Bmim][DCA] Flow Rates

The propulsive performance of a single capillary emitter was evaluated and a comparison of thrust and specific impulse as a function of [Bmim][DCA] flow rate was made. Figure 22 documents the theoretical thrust and specific impulse as a function of flow rate from the results presented above. The curves were generated by fitting and extrapolation of the experimental results at six volumetric flow rates ranging from 0.3 to 2.18 nL/s. The acceleration voltage was taken as the extraction voltage offset by the ohmic losses present in the emitted ions (not shown) and taken as 1793 V in all calculations and determined by using the RPA results of the m/q values greater than 1000 amu/q, which is expected to be the bulk of the charged species. As can be clearly seen in the figure, the presence of droplets greatly restricts the theoretical specific impulse, I_{SP}, which is limited to only 600 at the lowest end of the extrapolated flow rate curve at the capillary limit for this liquid, 4.35 pL/s. Measurements below 0.27 nL/s were not made in this experimental investigation, however, so the estimates are simply assumptions below this flow rate.
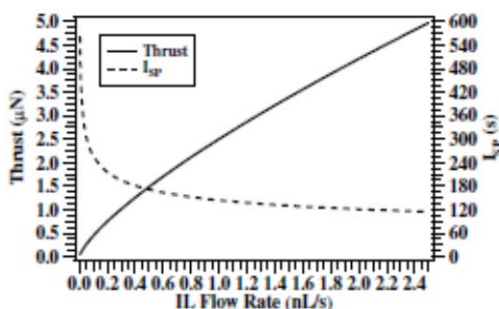
Figure 22: Predicted Propulsion Performance for a Single [Bmim][DCA] Capillary

4.6 MD Simulations of [Emim][Im]

In this section the results of a theoretical investigation into the electrospraying of [Emim][Im] were undertaken with the benefit of the numerous experimental insights that preceded it. In the journal publication [Emim][Im] was referred to as [Emim][Tf$_2$N], another abbreviation used for the same ionic liquid. We have chosen to keep it as [Emim][Im] owing to usage in previous sections, however, figures that appear in this section will likely bear the [Tf$_2$N$^-$] label that correspond to the Im$^-$ anion. The two anions are exactly equivalent and are simply two different ways for abbreviating the same species.

A number of important questions were developed to try and increase the microscopic understanding of the physical events that occur in the emission process. Examples of the key questions include: In light of the fact that [Emim][Im] has negligible vapor pressure, is evaporative cooling a likely mechanism for explaining the existence of the n = 2 cluster observed in experiment but thought to be thermally unstable? What are the differences between electric field induced dissociation and thermal induced dissociation for clusters of [Emim][Im]? What occurs energetically to ions that are emitted from a suitably sized droplet? Can MD qualitatively reproduce the ion distribution as it approximately had for the salt-formamide solutions? These questions will be addressed in the following paragraphs. This section relies on extensive calculations involving quantum mechanical and classical atomistic molecular dynamics simulations for which the details have not yet been provided in this report, but are available in detail in the published journal article on this topic. Interested readers should consult the article

for full accounting of the theoretical details and results. Only the key findings will be presented below.[6]

The first question that is addressed in this section is related to the thermodynamic stability of the ion clusters, particularly the n = 1 and 2 cation and anion clusters. To address this question, quantum mechanical (QM) calculations at the MP2 level with the 6-311++G(d,p) basis were performed to locate the minimum energy structure of the various clusters. Stationary points were validated by performing a Hessian analysis of the optimized geometry which outputted the calculated vibrational frequencies for the cluster. The internal energy at various temperatures was calculated by assuming a normalized vibrational and rotational Maxwell-Boltzmann energy distribution for a given temperature T. The results of this analysis for the n = 1 anion cluster are shown as the population fraction given as solid lines in Figure 23 for T = 300, 400, and 500 K.
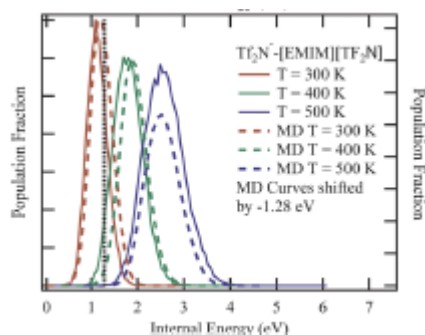
Figure 23: Internal Energy Analysis of the n = 1 Anion Cluster

The same QM calculations allow the direct calculation of the theoretical binding energy; the energy that would need to be input to break a cluster into two components. This energy is depicted in Figure 23 as the vertical dashed line at approximately 1.28 eV. Using the understanding presented in section 4.2, any cluster with internal energy greater than this vertical line is expected to dissociate (i.e. Im^- [Emim][Im] $\rightarrow$ Im^- + [Emim][Im]). For this cluster, the QM results indicate that approximately 35% of the ions would be expected to dissociate at 300 K and over 90% by 400 K. As observed in section 4.1, the experiments performed at 373 K show no changes in the n = 1 anion intensity. The dashed profiles in Figure 23 are generated from the calculated potential energy distribution at 300, 400, and 500 K minus the binding energy calculated from the QM results. Excellent agreement between the QM and MD thermochemistry verified the effectiveness of the force field used in the MD investigations.

The thermodynamic analysis of the binding energies and internal energies of the clusters, applied as recommended in section 4.2, provided predictions that n = 2 cation and anion clusters would not exist at all at 300 K and that the n = 1 clusters should result in significant dissociation. It is worth noting that these molecules consist of a fairly large number of atoms which directly correlates to a large number of vibrational states that can be populated and significant internal energies even at low temperatures. An alternate approach employing classical MD simulations was explored to simply simulate a thermally equilibrated cluster over a long simulation period, 40 ns, and evaluate the number of trajectories that lead to dissociation. An example of such an analysis is depicted in Figure 24 for the n = 1 and n = 5 cation species. The % of trajectories resulting in dissociation is plotted as a function of the equilibration temperature of the cation cluster. A sigmoidal profile is found for every cluster sampled with temperatures greater than 500 K necessary to result in dissociation. This result suggests that thermal induced dissociation

26

is not likely unless the emission point results in significantly larger temperatures than the room temperature of the liquid.
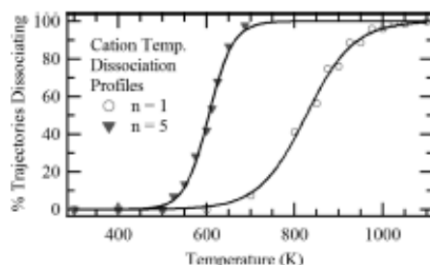
Figure 24: Cation Dissociation Profile

The trajectories based on the thermal investigation did reveal a number of related findings, including the products of the resulting dissociation and the effects on the temperature of the dissociated clusters. Thermal-induced breakup of the parent cluster into two clusters does result in evaporative cooling as reflected in the kinetic energy of the ion cluster before and after dissociation. Unfortunately, the dominant mechanism for breakup is found to be through the "n-1" channel, where a parent cluster simply sheds a single neutral pair with each cooling event. As such, to generate only n = 0, 1, and 2 clusters, several dissociation events would be required for larger *n* clusters and significant numbers of neutrals would be generated.

We investigated the difference between thermal and electric field induced breakup and noted a number of contrasting results with key results presented in Figure 25. The preferential mechanism for the electric field dissociation was the "n-n" pathway, where a parent cluster subjected to a significant electric field would generate an n = 0 cluster and a neutral droplet of n neutral pairs. Thus, generation of n = 0, 1 and 2 clusters from a large parent cluster would only require a single dissociation event. We also discovered that neutral clusters of [Emim][Im] require an electric field magnitude of approximately 0.985 V/nm to generate ion emission, in excellent agreement with the 1.0 V/nm experimentally determined. A reporting of the electric field strength required to dissociate small clusters is presented in the left panels of Figure 25. It can be seen that clusters greater than n = 2 experience at least 90% dissociation at field strengths of 1.0 V/nm suggesting that the non-appearance of higher *n* clusters in the low flow rate regime may result from too intense an electric field.
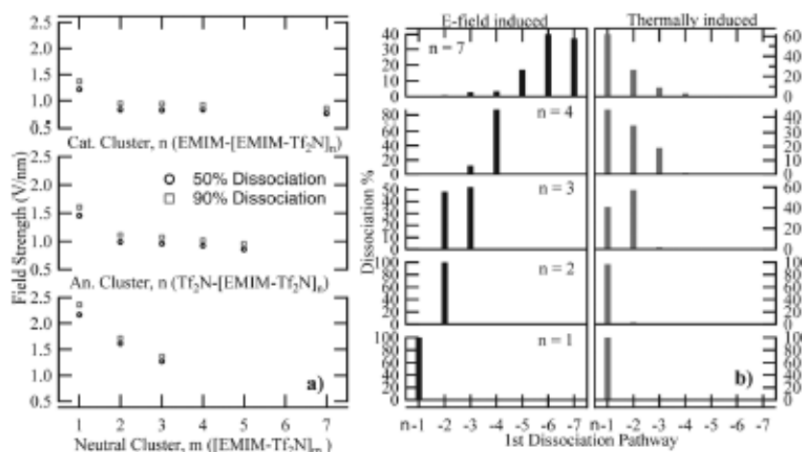
Figure 25: Electric Field Dissociation Profiles and Mechanism Comparison

While visualizing the conformation of the n = 2 anions that resulted in dissociating trajectories, it became clear that every single dissociation went through a gateway conformation before dissociating from the parent cluster.   To further understand this gateway, we identified three conformations near the dissociation event. These conformations are presented at the top of Figure 26 and reflect the leaving anion in three unique conformations relative to the dimer. The bottom panels of Figure 26 tabulate the MD and QM potential energy surface of the anion as it is moved further from the dimer in the fixed orientation. Figure 26a shows the potential energy surface calculated with no electric field active; all of the conformations have barriers amounting to at least 8 kcal/mol and excellent energy agreement between the MD and QM methods is highlighted in conformation 3. In 26b, the potential energy surface with a field of 0.9 V/nm is depicted. Orientation 1 and 2 still have an activation energy barrier to dissociation but it is significantly decreased relative to the values in a). Again excellent energy agreement between QM and MD are demonstrated, even with the application of the electric field in both cases. 25c) combines a) and b) and highlights the energy stabilizing effect of the electric field. The minimum energy is ~10 kcal/mol lower with the field than without the field. In the case of orientation 3, the barrier to dissociation has nearly disappeared indicating that dissociation to a single anion and a dimer is essentially isoenergetic in the presence of the electric field. 25d) highlights the importance of the magnitude of the electric field as a barrier of a couple of kcal/mol still exists at an electric field strength of 0.7 V/nm. These cuts along the surface indicate that the electric field allows access to areas of the potential energy surface simply not accessible to the thermal case. We confirmed that the n = 2 anion cluster in the absence of the electric field at 300 K simply never finds a similar orientation during a trajectory.
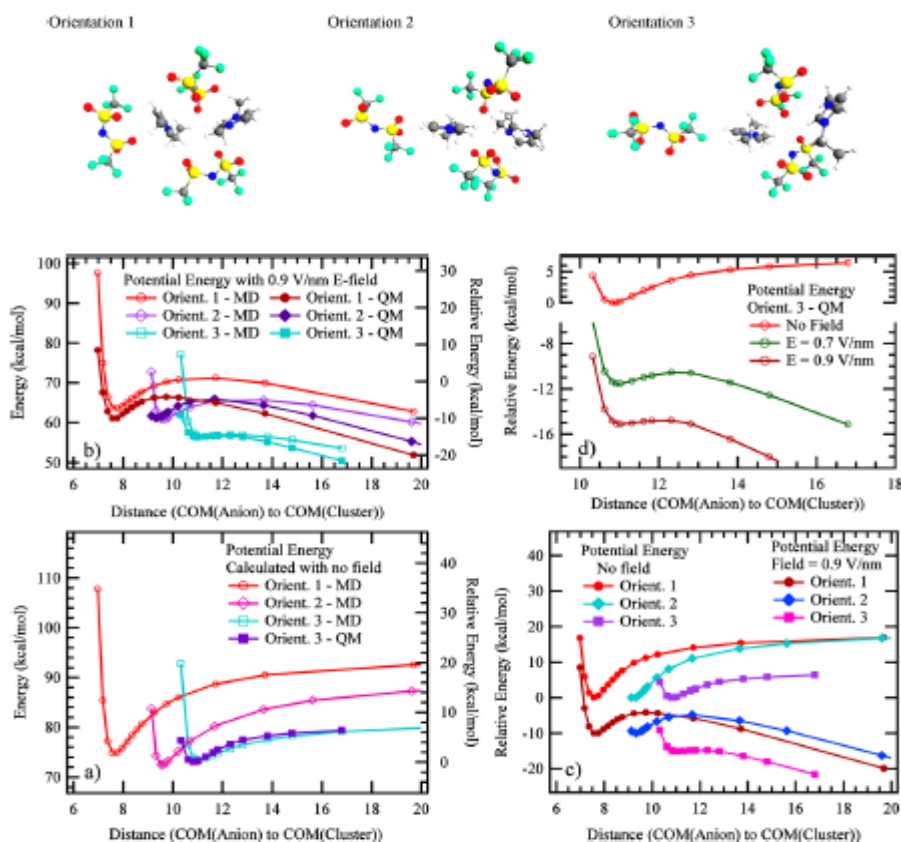
Figure 26: Potential Energy Surfaces of Dissociating Trajectories

4.7 Cross Sections for Xenon Electric Thruster Plasmas

In this section, fundamental measurements of the near-infrared optical emissions resulting from xenon ion collision with thermal xenon gas at ion kinetic energies of 100-900 eV are reported. The experimental apparatus was described in section 3.3. Full detailing of the methodology, results, and conclusions can be found in the full length journal article.[12] The key results and findings will be presented in the following paragraphs and those readers interested in a full accounting should consult the article. The optical cross sections reported in this section provide direct inputs to a physics based collisional radiative model that can be applied to xenon-propelled ion thrusters. The exact processes involved include:

$$Xe^+ + Xe \rightarrow Xe^{+*} + Xe^*, \quad Xe^{2+} + Xe \rightarrow Xe^{2+*} + Xe^*, \quad \text{and} \quad Xe^{2+} + Xe \rightarrow Xe^{+*} + Xe^{+*} \qquad (2)$$
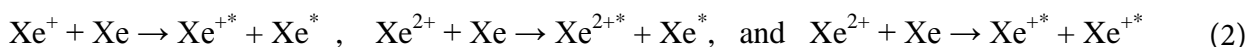
Emissions in the 300-1000 nm optical range are the most significant in the near-infrared, specifically between 788 nm and 992 nm which contain excited state neutral atomic xenon emission lines originating from the $5p^5 6p$ electronic state, termed the "2p" state in Paschen notation. These transitions consist of 11 different transitions in the NIR that directly couple to the 1st excited state ("1s"). The cross sections were measured for these transitions with energy spacing of 100 eV in the LAB frame after calibration of the optical setup to previously measured electron impact cross section values for the same transitions. The use of the calibration factor generates an uncertainty of 40% in the tabulated cross section values even though the systematic uncertainty (reproducibility) is typically below 15% except at the lowest energy values.

The emission excitation cross sections for the NIR transitions of neutral xenon are presented in Table 5 for the collision of Xe^+ + Xe and Table 6 for Xe^{2+} + Xe. The energy values in the left hand column indicate the laboratory kinetic energy of the ion and not the E/q value. As noted in the table title, the emission excitation cross section values should be multiplied by 10^{-18} to arrive at the proper value. The emission excitation cross sections increase significantly from 100 eV to 200 eV and continue to increase until roughly plateauing somewhere in the vicinity of 300-500 eV. The most intense transition observed is the 882 nm emission line which reaches a maximum cross section value of 68.9 at 800 eV. The Xe^{2+} + Xe data reflect similar trends but the emission excitation cross section of neutral xenon is considerably weaker than that observed for the single charge collision.

Table 5: Xe^+ + Xe Emission Excitation Cross Sections (x 10^{-18} cm^2)

Energy, eV	789 nm	823 nm	828 nm	835 nm	841 nm	882 nm	895 nm	905 nm	916 nm	980 nm	992 nm
100	0.112	10.1	2.6	0.729	0.832	29.3	3.67	11.5	6.05	18.1	17.4
200	0.416	17.8	2.9	2.16	1.16	45.3	6.49	19.6	19.4	30.1	28.4
300	0.475	25.4	3.27	2.85	1.55	54.6	8.55	23.6	24.8	39.7	36.5
400	0.493	26.1	4.42	2.94	1.86	57.8	10.5	25.0	32.1	34.8	37.7
500	0.547	32.1	5.49	3.49	2.08	60.4	11.2	25.8	42.5	42.0	45.0
600	0.464	31.2	4.97	3.67	2.12	62.0	11.2	24.8	39.0	39.6	35.1
700	0.515	33.3	4.79	3.82	2.28	62.0	11.9	25.2	36.5	36.0	38.0
800	0.573	38.1	5.22	4.18	2.66	68.9	13.6	29.1	45.6	38.1	42.8
900	0.589	37.9	5.14	4.11	2.57	66.5	13.7	27.3	42.6	34.1	40.3

29

Table 6: Xe²⁺ + Xe Emission Excitation Cross Sections (x 10⁻¹⁸ cm²)

Energy, eV	789 nm	823 nm	828 nm	835 nm	841 nm	882 nm	895 nm	905 nm	916 nm	980 nm	992 nm
200	——	3.15	0.676	1.17	0.36	6.99	1.22	1.83	2.3	1.51	1.52
400	0.27	5.14	0.872	1.98	0.606	9.9	2.06	3.65	6.04	4.27	5.4
600	0.425	6.80	1.17	2.54	0.877	12.8	2.69	4.17	7.88	6.75	6.26
800	0.376	6.17	1.03	2.49	0.702	11.4	2.56	3.83	6.89	4.05	5.00
1000	0.427	5.90	1.06	2.37	0.748	10.7	2.36	3.56	6.46	4.00	4.94
1200	0.398	5.64	0.982	2.43	0.740	11.4	2.31	3.93	7.12	4.35	5.62
1400	0.356	5.00	0.986	2.51	0.696	9.76	2.09	3.22	5.55	3.31	4.18
1600	0.449	6.08	1.11	2.44	0.728	10.5	2.29	4.03	7.09	4.99	5.60
1800	0.452	5.71	1.14	2.62	0.876	11.1	2.40	3.92	6.90	4.57	5.58

4.8 Large-angle Xenon Ion Scattering: Differential Cross Sections

Spacecraft integration of ion thrusters requires an understanding of the potential contamination effects that can occur from the propellant when the thruster is operational. In previous years, the charge-exchange cross section resulting from collision of Xe⁺ and Xe²⁺ ions with neutral, thermal xenon was published for a wide energy range. The results indicated that symmetric charge exchange is efficient for the reactions with cross sections near 100 Å² near thermal energies and ~50 Å² at 300 eV in the laboratory (thruster) frame of reference for the singly-charged ion.[17] Time-of-flight kinetic energy analysis indicated that the bulk of these collisions were elastic, no change in kinetic energy was experienced by the collision partners. Elastic scattering between xenon ions and xenon atoms can produce ion currents at large angles with respect to the axis of electrostatic thrusters. Since contamination hazards are normally handled through effective modelling of the thruster, experimental measurements are required to supply the inputs into the models. In this case, large angle scattering cross sections are determined by making differential scattering cross section measurements on the above reactions at selected energies. In addition, an estimate of the sputtering yield of the ions at ion thruster relevant energies provides an additional input, particular for collision of the ions with boron nitride and molybdenum surfaces which are typically employed in Hall thrusters as insulating materials. What follows in this section is a summary of key results and findings pertaining to the large-angle scattering processes. The experimental results provided here use the experimental apparatus described in section 3.2. For full accounting of the results, methods, and conclusions, the interested reader is directed to the full journal length article available in the literature.[7]

The Newton diagram for elastic scattering in symmetric ion-atom collisions is presented in Figure 27. v is the laboratory ion velocity, v' is the laboratory scattered ion velocity, v'(SCX) is the laboratory scattered ion velocity of charge exchange ions and u' and u'(SCX) are the corresponding scattered center-of-mass (CM) velocities. The inset at the top left defines the impact parameter, b, and laboratory scattering angle of an ion-atom collision. For symmetric ion-atom systems, the CM velocity is half of the laboratory ion velocity. The diagram indicates two scattering possibilities, one producing maximum transverse velocities at a CM scattering angle of 90 degrees and the other at approximately 30 degrees. Collection of those ions with large transverse velocities is accomplished through careful control of the radiofrequency (rf) amplitude applied.
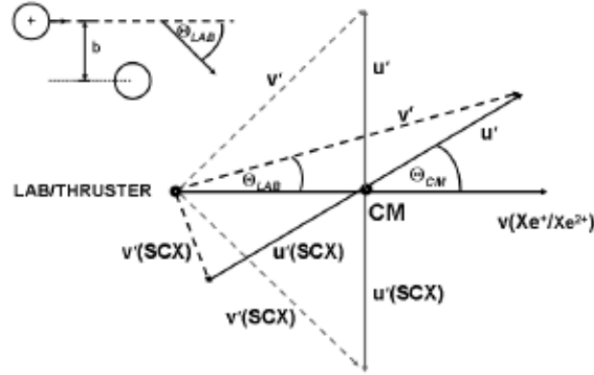
Figure 27: Newton Diagram for Elastic Scattering of Symmetric Ion-atom Collisions

Figure 28 depicts the velocity inverted TOF measurements plotted as intensity of signal versus laboratory velocity for Xe^+ + Xe collisions at laboratory ion energy of 5 eV. Two measurements are shown in 28(a) for high and low confinement fields corresponding to a maximum transmitted transverse velocity, v_t, of 2402 m s^{-1} (solid line) and 305 m s^{-1} (dashed), respectively. The two distributions are plotted on the same absolute vertical scale by ensuring that the total integrated intensity corresponds to the transmitted ion current at the corresponding rf amplitude. The vertical dashed line indicates the velocity of the system at CM. The large peak near 2700 m s^{-1} corresponds to the axial velocity of the primary beam and the second peak at near-thermal velocities is primarily attributable to charge exchange. Figure 28(b) presents a zoomed in view at smaller intensity values. At the low confinement field, those allowing only small v_t values, the overall ion transmission is reduced and no signal due to ions scattered at large angles appearing in the vicinity of the CM velocity is observed. As the octopole accepts ions with greater transverse velocities, measurement of increased signal at the v_{CM} increasingly becomes apparent. The signal at v_{CM} is reduced by ~1/2 at a confinement field corresponding to a maximum transverse velocity of 1403 m s^{-1} which corresponds to a transverse kinetic energy of 1.34 eV which, within experimental uncertainties, is in good agreement with the elastic maximum transverse ion energy of 1.25 eV.
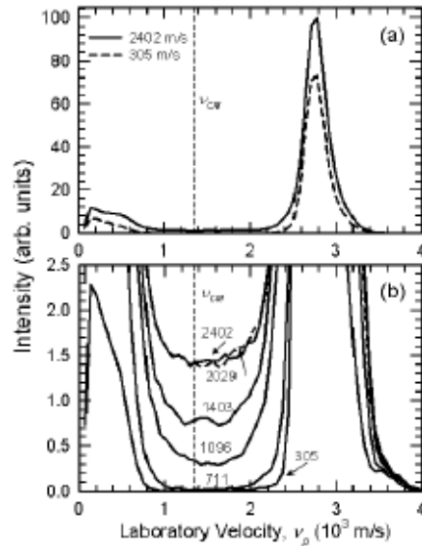
Figure 28: TOF Distributions of Xe$^+$ + Xe Collisions at Different Confinement Fields

Simulations of the differential scattering cross sections of the Xe^+ + Xe system were performed to allow direct comparison to measured experimental results. This was accomplished by fitting of the spin-orbit free interaction potentials of Xe^+ (^2P) with Xe obtained from the work of Paidarova and Gadea to a Morse potential functional form.[18] Full details of this analysis are available in the journal publication and only the summary of the results are reported here. The experimental data and the calculated velocity distribution using these potentials is depicted in Figure 29 for the Xe^+ + Xe collision at four ion energies. Excellent agreement between calculation and experiment is observed indicating the accuracy of the potentials used to derive the elastic scattering results.
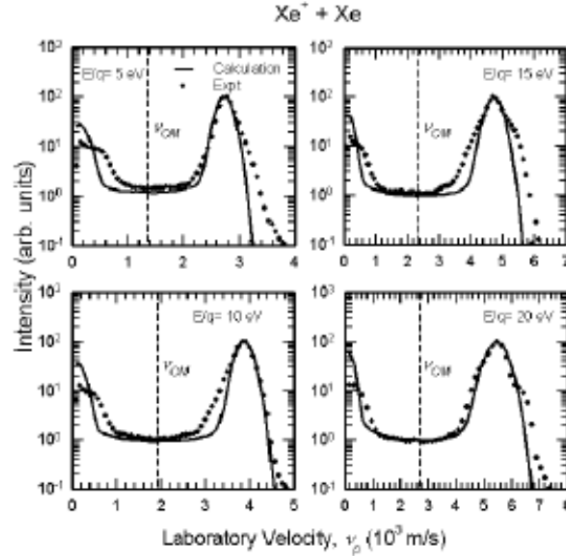
Figure 29: TOF Distributions for Xe^+ + Xe at Selected Energies

The interaction potential for the Xe^{2+} + Xe collision was not known at the time of publication. Using the agreement between the calculated and experimental data for the singly-charged collision, an interaction potential for Xe^{2+} + Xe was generated from best fitting of the combination potential:

$$V(R) = a_1(e^{a_2(a_1-R)^2} - 2e^{a_2(a_3-R)}) + (a_4 + a_5/R)e^{-a_6 R} \qquad (3)$$

where a_1-a_6 are fitted parameters to generate differential cross section values that best mimic the experimental data. The effective interaction potential, $V^{++}(R)$, used to reproduce the data is presented in Figure 30 along with the best fit parameters. Also shown are the Coulomb potentials associated with Xe^+ ($^2P_1$) + Xe ($^2P_1$), and the long-range polarization potential of Xe^{2+} + Xe, V^{++}_{pol} given by:

$$V^{++}_{pol}(R) = q^2 \alpha_d / 2R^4 \qquad (4)$$

where q is the atomic charge and α_d is the dipole polarizability of Xe (4.044 $Å^3$). The derived potential for doubly charged ion scattering is seen to be almost parallel with the Coulomb potentials between 3 and 4 Å above which it becomes more repulsive. The polarization and Coulomb potentials cross in the vicinity of 3 Å, which can be regarded as an interatomic distance where the electronic coupling is strong. The steep repulsive part of the derived potential for the

doubly-charged ion is also seen to be at significantly shorter distances than the effective singly-charged potential, $V^+(R)$, for scattering of singly-charged ions, in agreement with the lower differential cross sections at large angles for the Xe^{2+} collision system as compared to the Xe^+ system.

a_1	a_2	a_3	a_4	a_5	a_6
0.006	0.272	11.40	1500	0	3.737
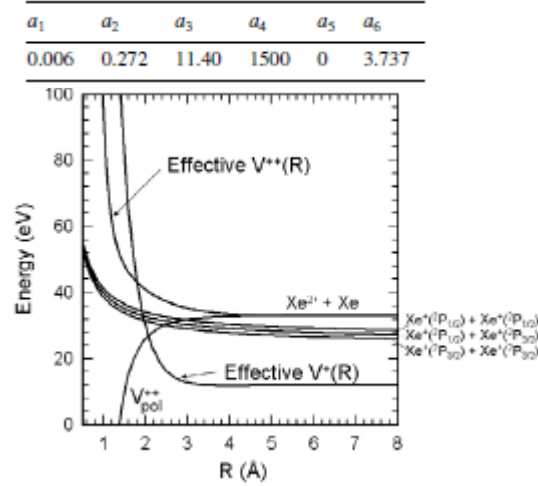
Figure 30: $V^{++}(R)$ Interaction Potential and Best Fit Parameters

A comparison of the laboratory differential cross sections for elastic scattering of $Xe^+ + Xe$ and $Xe^{2+} + Xe$ at a Hall thruster relevant ion energy of 270 eV is presented in Figure 31. For large CM scattering angles near 90°, the differential cross sections of the doubly-charged system are approximately a factor of 3 smaller than those of the $Xe^+ + Xe$ system.
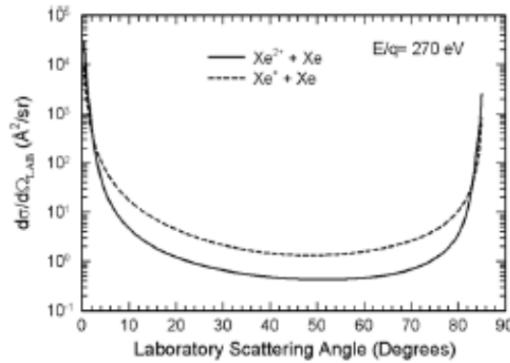
Figure 31: Laboratory Differential Cross Sections for Xenon Related Collisions at 270 eV

4.9 Xenon CRM: The Role of Metastable Atoms

Having previously measured the electron impact emission excitation cross sections related to xenon atoms at ion thruster relevant energies and combining those results with the measurements made in section 4.7, an attempt at the formulation of a physics based collisional radiative model covering all of the significant reactions leading to emissions from the 2p state of neutral xenon was now possible. In this section, the formulation of the collisional radiative model is described covering the emissions from electron-induced excitation in addition to the ion-induced excitation. Owing to the strength of the NIR transitions, the model will focus on

these transitions exclusively. One exception to this will be the re-excitation of the 1s metastable species, the $1s_3$ and $1s_5$ transitions in Paschen notation, which are not radiatively coupled the ground state configuration of neutral xenon and can be excited to higher lying excited states through low energy electrons. This re-excitation process leads to additional optical emissions since the excited states populated are coupled to radiatively-active states. Similar to previous sections, this work has been published as a full length journal article that will not be completely reproduced in this report. The interested reader is invited to consult the article for full consideration of the methods, results, and conclusions.[13] A subset of the important results and conclusions will be discussed below.

A schematic of the energy levels and electronic states of neutral xenon is presented in Figure 32. The ground state configuration of Xe is $5p^6$ while the first excited state consists of the 1s state (Paschen) with electronic configuration $5p^56s^1$. This level consists of four different states owing to spin-orbit coupling and are labeled $1s_5$-$1s_2$ where the greater the value of the subscript, the lower the energy relative to the other subscripts. The $1s_5$ and $1s_3$ states result in metastable population since they cannot radiatively couple to the ground state. This occurs because of selection rules relating to the need to change J (quantum number) in the transition to the ground state. The $1s_2$ and $1s_4$ states do radiatively couple to the ground state through optical emissions in the vacuum ultraviolet. Slightly above the 1s states in energy are the 10 2p transitions with electron configuration $5p^56p^1$. These 2p upper states couple to the 1s lower states through the wavelengths (in nm) depicted in the figure (e.g. 980 nm, 828 nm, etc.). Since the CRM will focus on the NIR lines other electronic states and their optical emissions will not be discussed.
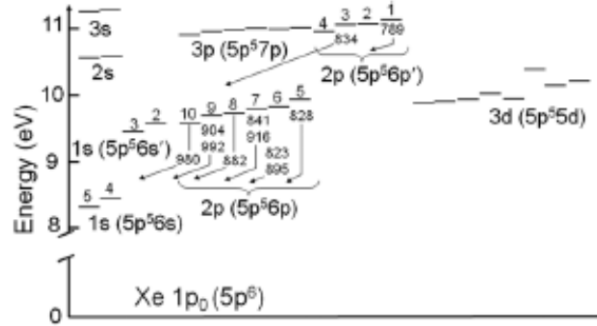
Figure 32: Schematic of Xe I Energy Levels

The KCD (Karabadzhak-Chiu-Dressler) collisional radiative model was developed to predict the relative intensities of the 11 NIR lines associated with $2p_i$ upper states of neutral xenon (Xe I). Given the very high radiative rates of the $2p_i$-$1s_j$ transitions, the model assumes that the $2p_i$ states are depopulated only through radiative transitions, and not through electronic collisional removal. Of the three $1s_j$ states associated with the NIR transitions, the $1s_5$ state is metastable with a lifetime of ~42 s.[19] Consequently, high excitation rates will lead to significant population of the $1s_5$ level, from which the $2p_i$ levels can be excited with significantly lower electron energies. According to Karabadzhak et al [20], the excitation rate of a particular NIR line at wavelength, λ, in energy units per steradian can then be expressed as

$$J_\lambda(XeI) = \frac{hc}{4\pi\lambda} N_o N_e \left(k_{e0}^\lambda + \frac{N_m}{N_0} k_{em}^\lambda + \alpha * k_1^\lambda + \frac{1-\alpha}{2} k_2^\lambda \right) \qquad (5)$$

where N_0 is the neutral atom number density, N_e is the electron number density, N_m is the metastable atom number density, $\alpha = N_1/N_e = N_1/(N_1 + 2N_2)$ is the ratio of singly charged ion density to the total ion density or electron number density, k_{e0}^{λ} is the ground-state atom electron impact line emission excitation rate coefficients, k_{em}^{λ} is the metastable-atom electron-impact line emission excitation rate coefficient and $k_1^{\lambda}/k_2^{\lambda}$ are the singly and doubly charged ion collision emission excitation rate coefficients. In equation (5), it is assumed that given the high ion energies at typical electrostatic thruster acceleration voltages, the difference between ion-induced ground-state atom and metastable atom emission excitation cross sections is not significant, and that excitation of ions by metastables can be neglected due to the much lower metastable densities in comparison with ground-state atom densities. The electron-temperature dependent rate coefficients are calculated through the usual means by convoluting the energy dependent cross sections with the collision velocity distribution:

$$k_e(T) = \left\langle f(E_e)\sigma_e(E_e)v_e \right\rangle_T, \tag{6}$$

where E_e is the electron energy, $f(E_e)$ is the normalized electron energy distribution, $\sigma_e(E_e)$ is the electron energy dependent excitation cross sections and v_e is the corresponding electron velocity. The model assumes a Maxwell-Boltzmann electron energy distribution. For ion excitation rates, a delta-function at the nominal accelerated ion energy is assumed:

$$k_{ion}(E_{ion}) = \sigma_{ion}(E_{ion})(2E_{ion}/m_{ion})^{1/2}, \tag{7}$$

where m_{ion} is the atomic mass of the ion.

The steady-state rate equation for population and depopulation of the 1s$_5$ metastable state can be written as

$$N_0 N_e \left(k_{0m} + \sum_i \left\{ k_{e0}^i + \alpha k_1^i + \frac{1-\alpha}{2} k_2^i \right\} \right) = N_m N_e \left(\sum_j P_j k_{2pm}^j + \sum_k k_{dm}^k + k_{ion} \right), \tag{8}$$

where on the right-hand side, representing depopulation rates, k_{2pm}^j, are metastable excitation rate coefficients to the 2p$_j$ levels, P$_j$ are the corresponding branching ratios for radiation from the 2p$_j$ level to the 1s$_4$ state that is optically coupled to the ground state and k_{dm}^k are metastable excitation rate coefficients to other atomic level manifolds for which repopulation rates to the 1s$_5$ state through radiative transitions can be neglected. The sum over j occurs for all upper states that are coupled to the ground state. The sum over k involves 1s$_5$ excitation rates to all other levels such as other 1s states, and 3d and 3p levels. k_{ion} is the 1s$_5$ electron-impact ionization rate coefficient. On the left-hand side, representing population rate coefficients, k_{0m} is the direct excitation rate from the Xe ground state. The sum on the left hand side of (8) is over emission excitation rate coefficients for which the lower states is the 5p^{5}6s $J = 2$ (1s$_5$) level. While these line emission excitation rate coefficients include cascade contributions, the right-hand side of equation (8) neglects cascades. The present calculations and experimental measurements by Jung *et al* justify the neglect of cascade contributions for the rate coefficients in terms on the right-hand side of equation (8)at the electron energies of interest.[21] The cross section

values used to generate the rate constants in (8) are taken from previous experimental work from this group including the cross sections reported in section 4.7. The electron impact cross sections were taken from previous measurements from this laboratory.[22] The cross section values used for the metastable excitation were taken from experimental measurements by Jung *et al* and calculations described in detail in the journal article.

The introduction of the metastable excitation rate coefficients alters the KCD model to either the BSR-RDW-Jung or BSR-RDW model depending on whether the $1s_5$-$2p_i$ cross sections are completed calculated (BSR-RDW) or are replaced, when available, with the experimental results of Jung *et al* (BSR-RDW-Jung). A direct comparison of the various models for two sets of observables is presented in Figure 33. In the left panel, the intensity ratio of the 823 nm to 828 nm emission lines is presented for the various models for a 300 V Hall Thruster as a function of electron temperature. The improved model results in predictions of lower ratios at all electron temperatures. In the right panel, the metastable fraction for both the models and an assumption of a Boltzmann distribution of metastables are compared. The improved models predict significantly less metastable fraction compared to the Boltzmann distribution.
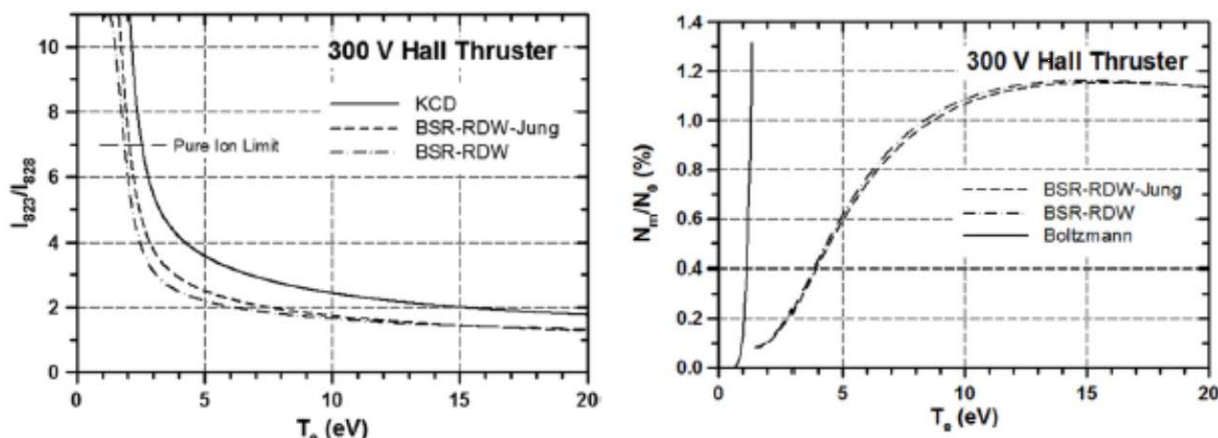
Figure 33: Comparison of Calculated Quantities for the CRM Models

Figure 34 shows model spectral fits to a TAL chamber measurement collected from an axial point that was 200 mm from the exit plane of the engine. Eight independent (unique upper states) NIR emission lines were chosen for the fit. The intensities are normalized and are shown on a logarithmic scale. The presently modelled spectral intensities exhibit a markedly improved comparison with experiment at the higher wavelengths of 882, 904, and 916 nm, while the KCD model provides a better agreement at 823 nm. Interestingly, a first upgrade of the KCD model consisting of introducing only the experimental $1s_5$-$2p_i$ excitation cross sections resulted in a complete failure of the model in reproducing the observed spectra assuming reasonable electron temperatures. This emphasizes the important of adding the de-excitation processes, $1s_5$-$1s_i$, $1s_5$-$3p_i$ and $1s_5$-$3d_i$, and $1s_5$-Xe^+, for which only theoretical cross sections are available.
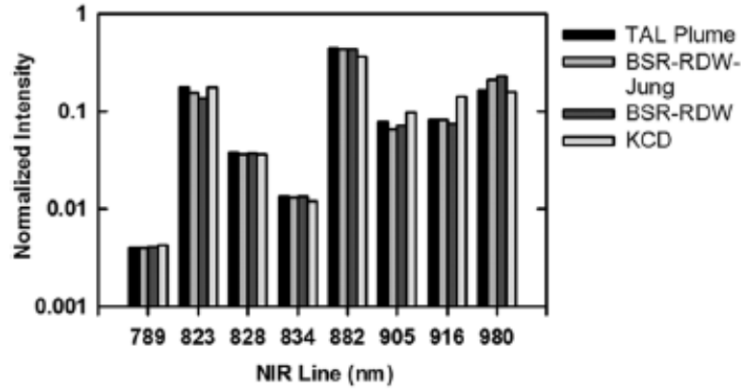
Figure 34: Comparison of a TAL Plume Compared with Calculated Intensities from CRM

A quantitative comparison of the model prediction of electron temperature to the values measured for a TAL thruster at 200 mm and 25 mm from the exit plane are presented in Table 7 for the 823/828 ratio, the 834/828 ratio, and the 8-line NIR fit. 823/828 and 834/828 refer to a 2-line analysis based on the respective intensity ratios. The 8-line analysis refers to a best fit to the intensities at the eight wavelengths shown in Figure 34. χ refers to the standard deviation of the 8-line analysis. Karabadzhak reported the TAL experimentally determined electron temperate at 300 mm was 3.0 eV.

Table 7: CRM Results of TAL Thruster

	T_e (eV)			
	823/828	834/828	8-line	χ
	200 mm			
KCD	3.4	2.8	3.4	0.284
BSR-RDW-Jung	2.5	2.8	2.7	0.124
BSR-RDW	2.3	2.8	2.6	0.176
	25 mm			
KCD	5.6	4.8	6.1	0.318
BSR-RDW-Jung	3.4	4.8	4.5	0.252
BSR-RDW	2.8	4.8	4.6	0.302

For additional evaluation of the upgraded model, optical emissions from a BHT-200 Hall thruster at various plume positions were recorded for the 823/828 nm pair. The BHT-200 HET operates at a slightly lower acceleration potential (250 V) than the TAL thruster sampled above which necessitates recalculation of the 823/828 ratio with the various models. The summary of experimental ratios and the calculated electron temperatures is presented in Table 8. The radial distance, r, is tabulated in units of the annulus outer diameter (OD = 3.2 cm). The I_{823}/I_{828} ratio is defined as the experimental intensity ratios. The columns for the various models are given in units of eV derived from the I_{823}/I_{828} ratio. Beal and coworkers report an axial electron temperate at $r = 0.156$ (50 mm) of 2.6 eV in excellent agreement with the BSR-RDW-Jung model predictions.[23]

Table 8: CRM Results for BHT-200 Hall Thruster

r (OD)	I_{823}/I_{828}	BSR-RDW-Jung	BSR-RDW	KCD
0	4.66	2.4	2.1	3.3
0.07	4.80	2.4	2.1	3.2
0.13	5.05	2.3	2.1	3.1
0.19	5.10	2.3	2.1	3.0
0.25	4.18	2.6	2.3	3.8
0.32	4.66	2.4	2.2	3.3
0.38	5.21	2.3	2.0	3.0
0.44	5.70	2.2	1.9	2.8
0.50	6.82	2.0	1.8	2.5
0.56	7.00	2.0	1.8	2.4
0.63	6.01	2.1	1.9	2.7

4.10 Laboratory Measurements of Kr^+/Kr^{2+} + Kr Emission Cross Sections

Xenon is by far the most common propellant in use on electric propulsion systems in operational space as of 2015. The limited availability and increasing cost of xenon coupled to the desire to evaluate alternate propellants in electric propulsion systems has led to increased research exploring these alternate propellants. One such propellant, Krypton, has been the subject of numerous investigations. Krypton is chemically similar to xenon; both are noble gases. The ionization energy of krypton is slightly higher than that of xenon and its atomic weight is slightly lower potentially leading to improved specific impulse. In this section, the emission excitation cross sections originating from electron-krypton collisions and krypton ion-krypton collisions are presented and discussed with the goal of providing crucial inputs to a krypton CRM. The specific reactions investigated include:

$$Kr^+ + Kr \rightarrow Kr^{+*} + Kr^* \tag{9}$$

$$Kr^{2+} + Kr \rightarrow Kr^{+*} + Kr^{+*} \tag{10}$$

$$Kr^{2+} + Kr \rightarrow Kr^{2+*} + Kr^* \tag{11}$$

$$e^- + Kr \rightarrow Kr^* + e^- \tag{12}$$

$$e^- + Kr \rightarrow Kr^{+*} + 2\ e^- \tag{13}$$
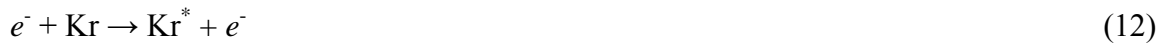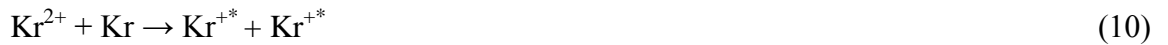
This investigation has been fully documented in a full length journal article and, as such, only the key results and findings are discussed in this section. The interested reader is directed to the full report available in the literature.[14] The results presented in this section were measured using the experimental apparatus described in section 3.3.

The electronic states of krypton have exact analogues to the ones presented in section 4.9 for xenon, albeit with different energy values. The ground state of neutral krypton has the electronic configuration of $4p^6$. The 1st excited state is termed the 1s state in Paschen notation and has the electronic configuration $4p^5 5s^1$ and consists of 4 levels termed $1s_5$ through $1s_2$ with

$1s_5$ being the lowest energy state. Similar to xenon, two of these states are metastable while the other two couple radiatively to the ground state. The second lowest lying is termed the 2p state in Paschen notation and has the electronic configuration $4p^5 5p^1$ and consists of 10 levels numbered $2p_{10}$ through $2p_1$ akin to that in xenon. Radiative emissions from $1s_2$ and $1s_4$ to the ground state occur in the vacuum ultraviolet while radiative emissions from the 2p states generally occur in the near-infrared, although at slightly different wavelengths than those observed in xenon. These NIR emissions were found to be the most significant emitters in the 250-1000 nm optical range. State specific information of neutral krypton related to the NIR is presented in Table 9. The upper state, lower state, branching ratio and wavelength of each transition are presented for the 16 NIR transitions. The branching ratios were taken from Aymar and Coulombe.[24]

Table 9: Krypton Emission Lines in the NIR

Upper State	Branching Ratio[a]	Lower State	λ, nm
$2p_5$	1.000	$1s_4$	758.7
$2p_6$	0.769	$1s_5$	760.1
$2p_1$	1.000	$1s_2$	768.7
$2p_7$	0.153	$1s_5$	769.5
$2p_3$	0.528	$1s_3$	785.5
$2p_4$	0.507	$1s_3$	806.0
$2p_8$	0.334	$1s_5$	810.4
$2p_9$	1.000	$1s_5$	811.4
$2p_6$	0.231	$1s_4$	819.0
$2p_2$	0.829	$1s_2$	826.3
$2p_3$	0.391	$1s_2$	828.1
$2p_7$	0.847	$1s_4$	829.9
$2p_4$	0.493	$1s_2$	850.9
$2p_8$	0.666	$1s_4$	877.7
$2p_{10}$	0.895[b]	$1s_5$	892.9
$2p_{10}$	0.105[b]	$1s_4$	975.2

The $Kr^+ + Kr$ collision system was first considered with a focus on the 18 emitting neutral Kr (Kr I) 2p states. Measurements over the energy range of 25 eV to 600 eV were investigated (12.5 to 300 eV in the center-of-mass frame of reference). The measured cross section values are presented in Table 10. The cross sections rapidly increase from the small values observed at $E_{cm} = 12.5$ eV and generally increase over the entire energy range sampled with increasing collision energy.

Table 10: $Kr^+ + Kr$ Emission Excitation Cross Sections ($x10^{-18}$ cm^2) for the Kr I 2p States

Energy eV, E_{cm}	975 nm	893 nm	877 nm	850 nm	829 nm	828 nm	826 nm	819 nm	811 nm	810 nm	806 nm	785 nm	769 nm	768 nm	760 nm	758 nm	587 nm	557 nm
12.5		0.27	0.11	0.14	0.05	0.08	0.10		0.38	0.18			0.03		0.19	0.01		0.00
25	1.86	15.20	14.00	1.57	7.68	0.98	3.57	2.09	19.60	13.00	1.46	1.55	1.36	0.34	7.65	1.31	0.29	0.22
50	4.09	29.10	25.30	4.89	12.70	2.68	10.70	5.68	43.10	12.60	4.23	4.29	1.94	0.95	20.40	4.46	0.77	0.58
100	5.57	41.72	35.89	6.96	23.18	5.07	15.73	10.64	46.11	35.07	6.21	8.19	3.57	2.49	36.89	8.03	1.21	1.16
150	6.61	45.40	47.90	9.15	29.80	5.39	20.10	12.20	69.30	25.50	7.72	9.22	4.72	2.41	42.90	7.15	1.44	1.32
200	7.04	51.00	48.20	9.57	33.60	5.48	20.30	15.70	76.70	22.80	8.38	11.30	5.74	3.09	52.70	7.96	1.57	1.52
250	6.81	46.50	51.10	8.54	35.50	6.21	20.80	14.40	70.80	25.10	7.16	9.86	5.52	4.22	49.70	7.70	1.64	1.46
300	6.89	48.40	55.80	9.25	37.90	5.86	21.10	15.50	78.50	25.70	7.92	9.86	6.13	4.78	52.60	8.41	1.64	1.41

The $Kr^{2+} + Kr$ collision system was then considered with a focus on the same 2p states of Kr I. Measurements over the energy range of 100 eV to 1200 eV were investigated (50 eV to 600 eV in the center-of-mass reference). Generally, for the same center-of-mass collision energy, the cross sections for Kr I are roughly a factor of 10 less for the Kr^{2+} induced emission than for those generated by Kr^+ collisions.

Table 11: Kr^{2+} + Kr Emission Excitation Cross Sections (x 10^{-18} cm^2) for the Kr I 2p States.

Energy eV, E_{cm}	975 nm[a]	893 nm	877 nm	850 nm	829 nm	828 nm	826 nm	819 nm	811 nm	810 nm	806 nm	785 nm	769 nm	768 nm	760 nm	758 nm
50	[0.19]	1.60	2.08		1.24	0.41	1.30	0.81	4.69	1.77	0.49	0.56			2.77	0.48
100	[0.34]	2.92	3.38	0.54	2.18	0.41	1.69	0.91	6.11	2.13	0.41	0.56	0.38	0.11	3.75	0.55
200	[0.39]	3.35	4.45	0.52	3.03	0.52	2.08	1.09	6.72	2.87	0.51	0.79	0.69	0.28	4.61	0.73
300	[0.44]	3.71	4.73	0.74	3.63	0.53	2.50	1.35	7.97	2.83	0.63	0.78	0.57	0.37	5.49	0.83
400	[0.39]	3.35	4.59	0.76	3.44	0.50	2.38	1.18	7.39	2.65	0.59	0.70	0.59	0.31	5.00	0.69
500	[0.42]	3.60	4.93	0.78	3.78	0.59	2.53	1.40	7.82	2.74	0.71	0.80	0.65	0.41	5.39	0.86
600	[0.40]	3.39	4.34	0.73	3.54	0.44	2.44	1.34	8.11	2.73	0.70	0.82	0.65	0.32	5.38	0.74

[a] Emission excitation cross section calculated using the theoretical branching ratio of 0.105

Figure 35 presents a number of other significant measurements of the Kr$^+$ + Kr collision system related to the various electronic states sampled in the 300-1000 nm optical range. In Fig. 35a, emission excitation cross sections from two different 2p upper states are depicted. The emission excitation cross section values for the transitions at 895.9 and 975.2 nm have been summed together to construct the energy dependence for the 2p$_{10}$ upper state. Similarly, the 2p$_3$ upper state energy dependence has been constructed by summation of the emission excitation cross section values associated with this upper state, notably the transitions at 785.5, 828.1 and 557.1 nm. The summed 2p$_3$ emission excitation cross section value is multiplied by 3.23 in Fig. 35a for ease of comparison. Qualitatively, the energy-dependent emission excitation cross sections for the emission from the 2p$_{10}$ and 2p$_3$ states are similar. This relationship qualitatively holds for all 2p$_x$ transitions with possible exception of 2p$_1$. The only 1s$_x$ ← 2p$_1$ transition is located in close proximity to the 2p$_7$ 769.5 nm transition and is the minor component of a doublet of peaks.   The emission excitation cross sections for the 1s ← 2p transitions are found to be very near zero at E_{cm} = 12.5 eV and rapidly increase until about E_{cm} = 200 eV where they are constant through 300 eV.

In Fig. 35b, emissions, in the 350-1000 nm range, from the 3d, 4d, 5d, 6d, 3s, 2p, and 3p transitions of Kr I and emissions resulting from various Kr II states (both ^{3}P and ^{1}D) are presented. The traces were generated by direct summation of all transitions originating from the electronic configuration and normalized such that the value at E_{cm} = 150 eV was unity. Initial emission from Kr II is observed at higher collision energies than all of the Kr I emitting states. The growth after onset appears to be approximately linear and continuing to grow at the highest energies investigated. All of the Kr I electronic states resulting from collisions of Kr$^+$ + Kr, viewed through their emission excitation cross sections in the 350-1000 nm range, have similar collisional energy profiles. A comparison between the cascade into and out of specific 2p states is presented in Fig. 35c. "X" denotes the 1s states that result from emission from the 2p$_x$ state while "Y" indicates the summed emission excitation cross sections of any higher lying state, in the 350-1000 nm range, that leads to the specific 2p$_x$ state. The cascade emission excitation cross sections from "Y" to 2p$_x$ have been multiplied by various factors for ease of comparison to the intense emissions from the 2p$_x$ states. In general, the "Y" to 2p$_x$ transitions, in the 350-1000 nm spectral range, make up only about 3-10% of the total emission excitation cross section observed for the 2p$_x$ states. Qualitatively, the energy-dependence of the emission excitation cross sections for these cascading transitions closely resembles those for the 1s ← 2p transitions.
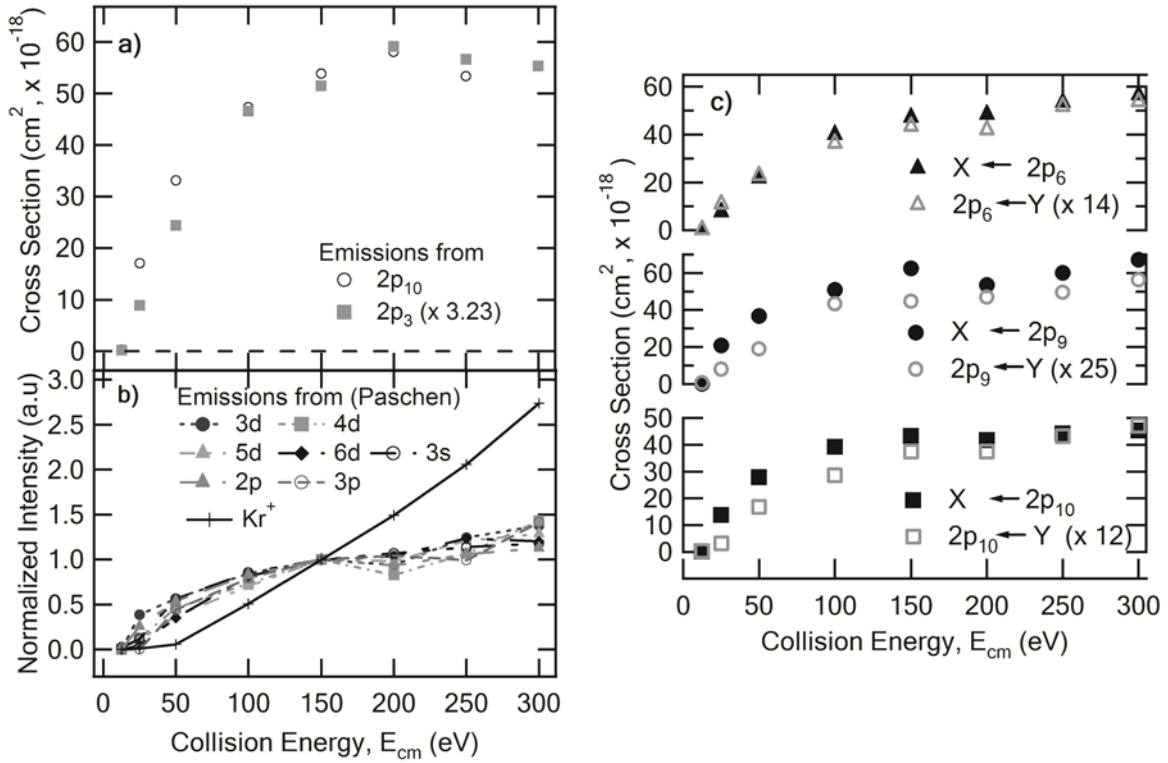
Figure 35: Kr$^+$ + Kr Electronic State Emission Profiles

The zero-pressure corrected emission excitation cross sections for the NIR emissions of Kr I resulting from electron impact at selected energies are presented in Table 12. The zero pressure emission excitation cross sections were calculated from performing a series of pressure dependent measurements and monitoring the intensity of the emissions. Using the formalism of Chiu *et al*, who proposed a semi-empirical expression for the relationship between the cross section value for a given electron energy, *E*, and pressure, *P*, and that for the same electron energy and zero pressure given by (for $E > 13.36$ eV):

$$\sigma_t(E,P) = \sigma_t(E,0)\left[1 + a\left(\frac{E-13.36}{E-11.76}\right)^n \left(1 - e^{-yP}\right)\right] \tag{14}$$

where $\sigma_t(E, P)$ is the cross section measured at the specific electron energy and pressure, $\sigma_t(E, 0)$ is the zero pressure emission excitation cross section. *a, n,* and *y* are fit parameters which are derived from varying the pressure from 0.1 millitorr to 3.0 millitorr for electron energy of 100 eV and measuring the $\sigma_t(E, P)$ values. *n* was fixed at a value of 1 to reduce statistical uncertainty in the fits. Efficacy of the approach is verified by comparing the fit parameters of the transitions which share a common upper state and who should have identical pressure dependencies. Finally, the branching ratio can be used to validate the effectiveness of the spectral sensitivity correction since the branching ratio of a common upper state must remain fixed independent of the electron energy. The experimental branching ratio was calculated by measuring the branching ratio at each electron energy and then averaging the results. The standard deviation is

41

the standard deviation of these individual values. Excellent agreement between theoretical and experimental branching ratios is observed.

Table 12: e⁻ + Kr Zero Pressure Emission Excitation Cross Sections (x 10^{-19} cm^2) for Kr I Best Fit

E_{cm} (eV)	975 nm 2p$_{10}$	893 nm 2p$_{10}$	877 nm 2p$_8$	850 nm 2p$_4$	829 nm 2p$_7$	828 nm 2p$_3$	826 nm 2p$_2$	819 nm 2p$_6$	811 nm 2p$_9$	810 nm 2p$_8$	806 nm 2p$_4$	785 nm 2p$_3$	769 nm 2p$_7$	768 nm 2p$_1$	760 nm 2p$_6$	758 nm 2p$_5$
13.71	4.29	31.45	37.18	4.75	12.54	3.70	27.11	10.06	70.75	18.58	5.40	6.33	2.28	12.88	34.85	36.62
15.84	4.54	33.02	37.52	6.03	8.87	5.19	40.78	12.08	93.05	21.72	6.07	7.34	1.48	17.34	34.24	32.01
17.83	5.18	38.90	43.49	7.28	9.73	6.24	52.13	14.56	110.75	25.67	7.39	9.58	1.72	20.91	40.21	34.20
19.97	4.78	36.11	42.17	6.87	9.34	5.95	52.51	14.12	101.51	26.01	7.03	9.29	1.62	20.55	46.74	32.99
21.92	4.20	31.62	39.70	6.07	8.78	5.28	48.86	13.05	86.75	23.50	6.14	8.35	1.55	19.74	42.71	31.25
23.75	4.23	31.19	44.14	6.05	9.22	5.35	51.64	13.62	84.57	24.62	6.07	8.21	1.63	20.70	44.36	33.04
29.1	3.12	23.48	37.39	4.35	8.29	3.99	42.46	10.93	56.71	20.32	4.43	6.08	1.46	18.26	36.33	29.70
34.4	2.47	18.89	35.65	3.51	8.18	3.21	37.84	9.53	42.72	18.60	3.51	4.82	1.44	17.95	32.49	29.92
39.25	2.14	16.78	36.17	3.08	8.40	2.70	35.06	8.66	34.44	17.54	3.02	4.03	1.50	18.54	29.89	31.09
48.6	1.86	14.34	36.08	2.73	9.06	2.54	33.22	7.95	26.58	17.52	2.63	3.33	1.61	20.62	26.10	34.34
58.8	1.60	12.23	33.54	2.36	8.60	2.12	28.81	6.77	20.43	15.66	2.24	2.59	1.53	19.72	24.92	33.18
78.8	1.35	10.48	29.68	2.03	8.05	1.67	23.47	5.57	15.11	13.87	1.94	2.12	1.41	18.32	21.33	30.83
100	1.26	9.84	28.39	1.69	7.42	1.50	19.50	4.64	11.37	12.03	1.62	1.72	1.30	16.55	17.83	27.67
148	1.26	9.49	26.71	1.88	7.80	1.51	18.59	4.69	12.05	12.38	1.78	1.91	1.40	17.08	18.38	28.93
a	3.88	3.89	2.34	5.36	10.79	4.20	0.98	1.81	3.27	2.36	5.60	4.80	10.86	1.18	1.74	2.11
n	1	1	1	1	1	1	1	1	1	1	1	1	1	1	1	1
y	0.49	0.49	0.58	0.38	0.72	0.26	0.23	0.45	0.14	0.55	0.30	0.26	0.72	0.30	0.49	0.45
Theo.BR	0.105	0.895	0.666	0.493	0.847	0.391	0.829	0.231	1.000	0.334	0.507	0.528	0.153	1.000	0.769	1.000
Expt. BR	0.117	0.883	0.658	0.501	0.850	0.379		0.228	1.000	0.342	0.499	0.540	0.150	1.000	0.772	1.000
St. dev.	0.002	0.002	0.026	0.012	0.002	0.026		0.018	0.000	0.026	0.012	0.026	0.002	0.000	0.018	0.000

4.11 Measurement of the Charge Exchange Cross Sections of Kr Ions

Effective modeling of the plume of a krypton ion thruster requires an understanding of the charge-exchange cross section involving ions with neutrals likely to occur in the operation of the ion thruster. In addition to the magnitude of the charge-exchange cross section, an understanding of the energy transfer that occurs between ion and neutral is also important. In this section the charge exchange cross sections of reactions (9), (10), and (11) are measured for laboratory frame energies of 1 eV to 300 eV. In addition, time-of-flight measurements provide insight into the degree of kinetic energy transfer that occurs upon collision of the partners. Only the key findings and results will be discussed in this section and the interested reader is directed to the full length journal article available in the literature. The experimental results presented in this section use the experimental apparatus discussed in section 3.2.

Figure 36 details the value of the symmetric charge exchange cross sections for Kr$^+$ + Kr and Kr^{2+} + Kr from the present measurements obtained through the attenuation method and plotted against a number of other reported measurements. The Gadea potentials are calculated from the Spin-orbit included Kr$_2^+$ interaction potentials of Gadea *et al.*[25] Attenuation data can overestimate the cross section due to loss of the primary beam scattered at large angles. Below 2 eV, the blocking potential applied to the second octopole was reduced, which may, in this case, allow additional products to pass thus lowering the cross section value obtained. For the singly-charged ion, the cross section is approximately 90 Å^2 at 0.2 eV E_{cm} and drops to approximately 40 Å^2 at 150 eV E_{cm}. The cross section measured for the symmetric doubly-charged reaction ranges from approximately 45 Å^2 at 1 eV E_{cm} to 20 Å^2 at 300 eV $E_{cm.}$
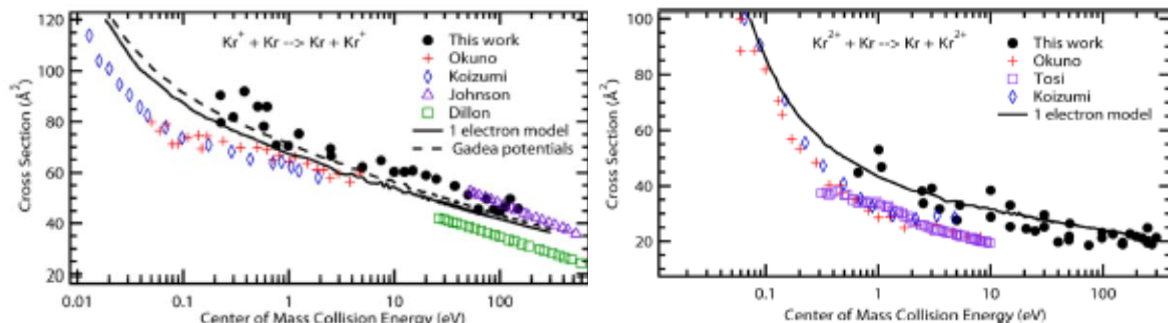
Figure 36: Symmetric Charge Exchange Cross Section for Kr$^+$ + Kr and Kr^{2+} + Kr

The asymmetric charge exchange cross section for the collision of Kr^{2+} + Kr resulting in the formation of Kr$^+$ and Kr$^+$ is presented in Figure 37. These values were measured using the branching ratio approach described in section 3.2. The cross section values indicate this channel is only a minor component of the total charge exchange with a value of approximately 1.6 Å^2 above E_{cm} = 10 eV. The cross section values below E_{cm} = 7 eV are believed to be a simple offset and reflect the baseline of the instrument response. Apart from an apparent, reproducible increase of signal around E_{cm} = 90 eV, the asymmetric charge exchange cross section remains effectively flat once appearing, up to at least E_{cm} = 300 eV.
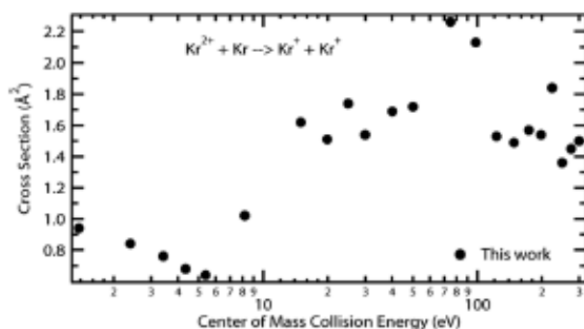
Figure 37: Asymmetric Charge Exchange Cross Section for Kr^{2+} + Kr

The cross section profiles for symmetric charge exchange were fit to a function of the following form:

$$\sigma^{SCX} = A - B \log(E), \tag{15}$$

where σ^{SCX} is the symmetric charge exchange cross section value, E is the collision energy in the laboratory frame of reference, and A and B are fitted parameters used to reproduce the energy dependence of the symmetric charge exchange cross section. The results of this fitting are presented in Table 13 for xenon and krypton. The fit parameters are very similar for the two atomic species for both single and double charge symmetric charge exchange. As expected, the Kr cross sections are slightly smaller than that of Xe, likely due to the smaller size and smaller polarizability for Kr. Interestingly, the slope of the both Xe and Kr is the same within the error bars of the two fits.

Table 13: Best Fit Parameters for Kr and Xe Symmetric Charge Exchange

	A (Å^2)	B (Å^2)
Xe$^+$ + Xe	87.3 ± 0.9	13.6 ± 0.6
Xe^{2+} + Xe	45.7 ± 1.9	8.9 ± 1.2
Kr$^+$ + Kr	80.7 ± 1.2	14.7 ± 0.8
Kr^{2+} + Kr	44.6 ± 1.7	9.8 ± 0.9

4.12 Measurement of the Charge Exchange Cross Section of Iodine Ions

Another alternative propellant to xenon for use in ion thrusters is Iodine. Iodine, unlike xenon and krypton, is a solid at room temperature and exists as a diatomic molecule in the standard state, as compared to the gaseous xenon and krypton. Iodine is significantly more prevalent on Earth than the two gases. Atomic iodine has a similar atomic mass to xenon (126.9 to 131 amu) and similar effective ionization potential (IP) (11.99 eV, 9.3 for ionization of molecular iodine and a further 2.68 eV to dissociate into I^+ + I) to xenon (12.12 eV) suggesting that the iodine propellant may not require complex retooling of the thruster, with the exception of a heating system to generate iodine vapor. In addition to the ion thruster related motivation, the reaction of I_2^+ + I_2 features a symmetric charge exchange reaction that involves two different molecules, as opposed to the more common ion-atom reactions. In this experimental report, charge-exchange cross sections, branching ratios, and time-of-flight analysis are reported for two collision systems with two potential product formations:

$$I_2^+ + I_2 \rightarrow I_2 + I_2^+ \ / \ I_2 + I^+ + I \tag{16}$$

$$I^+ + I_2 \rightarrow I + I_2^+ / I + I^+ + I. \tag{17}$$

These experiments are conducted on the experimental apparatus described in section 3.2. Full accounting of the methods, results, and conclusion are the subject of a full-length journal article available in the literature and, as such, only the key results and conclusions are discussed here.[9]

The charge exchange cross section for the iodine collision systems are presented for Lab energies ranging from 0.5 to 300 eV in Figure 38. The black dots present the total cross section obtained from attenuation of the primary ion beam and the error bars are one standard deviation of a series of four or five measurements. The green diamonds are the cross section determined for the I_2^+ thermal product using time-of-flight methods while the blue diamonds are the cross section determined from using time-of-flight methods on the I^+ product. The red diamonds indicate the sum of the two TOF results. The time-of-flight measurements will be discussed further below. For the I_2^+ + I_2 collision, the total cross section appears to be approximately 125 Å^2 at 0.5 eV and decreases until approximately 5 eV to about a value of 65-75 Å^2 where it maintains an approximately constant value over the entire range sampled. The TOF sum results indicate the total cross section is ~105 Å^2 at the lowest collision energies and 40 Å^2 near 150 eV. As can be seen, the summed TOF results are systematically below the values obtained with the attenuation experiments, and we believe this is due, in the TOF experiments, to inefficient collection of the product ions with thermal profiles, which occurs in the I_2^+ charge exchange product, as discussed below. In the case of I^+ + I_2, the total cross section appears generally lower

with the attenuation results suggesting a value of 98 Å^2 at the lowest energies and a near constant value of 55 Å^2 above 8 eV (LAB).
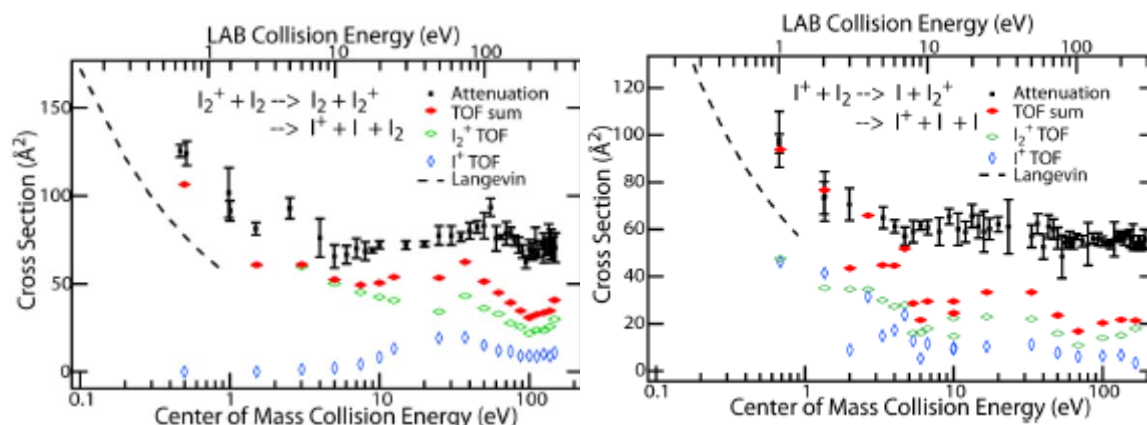

Figure 38: Charge Exchange Cross Sections for the Iodine Collision Systems

Figure 39 contains the collision induced dissociation cross section for the reaction of I_2^+ + I_2. Data is obtained using two different methods, the branching ratio method and the time-of-flight method. The branching ratio data are believed to be more reliable as the primary and product signals are collected near simultaneously unlike the TOF experiment, which requires a separate TOF measurement of both the product ion, I^+, and the primary ion, I_2^+. However, in this particular case, the cross section agreement between the two methods is excellent and, as will be shown below, is likely due to the fact that the I^+ product has kinetic energies significantly greater than thermal and is likely efficiently captured in the TOF experiment. As can be seen in the figure, at the lowest collision energies (< 3 eV), there is little to no reactive signal at all. This result is to be expected from the thermodynamics since I_2^+ dissociation is 2.68 eV endothermic. The cross sections starts to depart from zero value at 3 eV as expected. Once above the dissociation energy, the cross section increases to above 18 Å^2 between 25 and 37.5 eV (center-of-mass frame). From this point, the cross section decreases to a value of 8 Å^2 at the highest sampled collision energies.
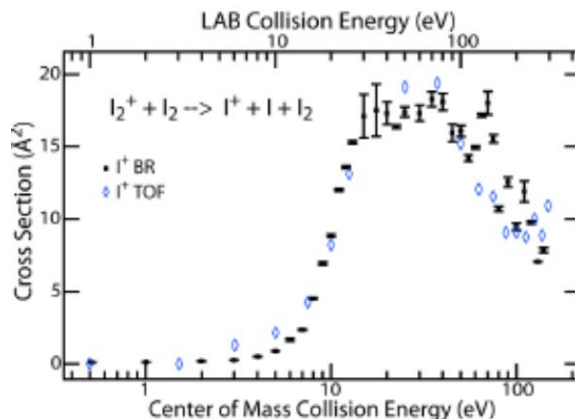

Figure 39: Branching Ratio/Time-of-Flight Comparison for the I^+ Product of I_2^+ + I_2

A typical time-of-flight spectrum for the I_2^+ + I_2 collision system is presented in Figure 40. In this figure, the primary ion beam, shown in green, has the shortest flight time. The center-

45

of-mass translational energy is 7.5 eV in this typical spectrum. The red curve is the TOF obtained for monitoring I_2^+ in the presence of the target gas. The short flight time ions in the red trace overlap the primary ion trace in green indicating these are unreacted primary ions. The distribution and long tail that occurs at 0.5 µs and continues to longer flight times are the formation of thermal I_2^+ product. The black curve depicts the time-of-flight profile for the I^+ product. In this collision system, the I^+ product appears to have the kinetic energy profile of the primary I_2^+ beam with no evidence of lower kinetic energies indicating the I^+ product originates from the collision induced dissociation of the primary I_2^+ ion and not through dissociative charge transfer of the neutral I_2 target gas.
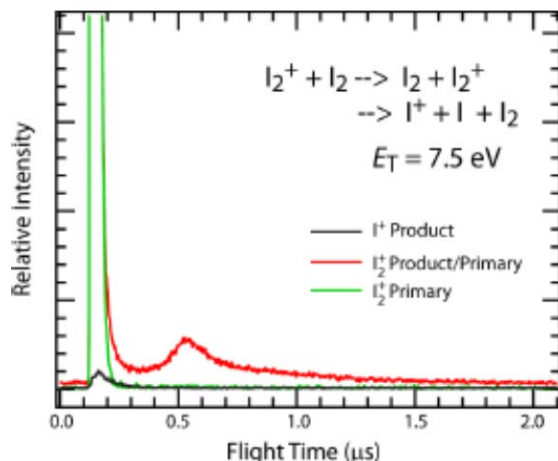

$$I_2^+ + I_2 \rightarrow I_2 + I_2^+$$
$$\rightarrow I^+ + I + I_2$$
$$E_T = 7.5 \text{ eV}$$

— I^+ Product
— I_2^+ Product/Primary
— I_2^+ Primary

Figure 40: Typical TOF Spectrum of $I_2^+ + I_2$

4.13 O^+ (^4S) + NH$_3$ Collision System at Hyperthermal Energies

Hyperthermal reactions of atomic cations with ammonia are interesting both from a fundamental standpoint, in the ongoing efforts to understand the detailed mechanisms of chemical reactions, and in a broader physical sense, for example, in the quest to understand the interactions of one of the important molecules in interstellar media. Modern computational methods are becoming powerful tools for studying chemistry and directly benefit from having experimental benchmarks for comparison. In a literature report of direct dynamics simulations by Sun and Schatz[26] on the O^+ + CH$_4$, excellent agreement was found with experiments on hyperthermal reactions of O^+ (^4S) + CH$_4$ performed in our group.[27] The aim of this section is to provide a further basis of comparison for theoretical work. The experimental results presented here utilize the experimental apparatus described in section 3.2 to measure the absolute cross section for the reaction of ground-state O^+ with ammonia at collision energies in the range from near-thermal to approximately 15 eV. These results are also the subject of a full length journal article and readers wishing for complete coverage of all methods, details, results and conclusions are encouraged to read the journal publication.[10] What follows in the remainder of this section is a presentation of the key findings.

In this section, we present the results of a GIB study of the O^+ + NH$_3$ reaction system, in which we have measured absolute cross sections for the observed reaction channels at near-thermal to hyperthermal collision energies. We have also determined recoil velocity distributions for product ions at selected collision energies. Experiments were carried out using normal and

perdueteroammonia because of the prospect of coincident ion masses. The product channels and their associated ground-state energetics are listed below for the exothermic channels:
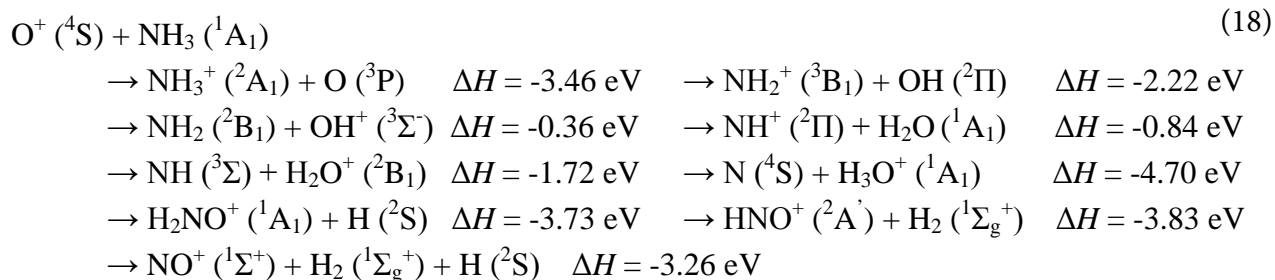
$$O^+ (^4S) + NH_3 (^1A_1) \tag{18}$$

$$\rightarrow NH_3^+ (^2A_1) + O (^3P) \quad \Delta H = \text{-3.46 eV} \qquad \rightarrow NH_2^+ (^3B_1) + OH (^2\Pi) \quad \Delta H = \text{-2.22 eV}$$

$$\rightarrow NH_2 (^2B_1) + OH^+ (^3\Sigma^-) \quad \Delta H = \text{-0.36 eV} \qquad \rightarrow NH^+ (^2\Pi) + H_2O (^1A_1) \quad \Delta H = \text{-0.84 eV}$$

$$\rightarrow NH (^3\Sigma) + H_2O^+ (^2B_1) \quad \Delta H = \text{-1.72 eV} \qquad \rightarrow N (^4S) + H_3O^+ (^1A_1) \quad \Delta H = \text{-4.70 eV}$$

$$\rightarrow H_2NO^+ (^1A_1) + H (^2S) \quad \Delta H = \text{-3.73 eV} \qquad \rightarrow HNO^+ (^2A^{'}) + H_2 (^1\Sigma_g^+) \quad \Delta H = \text{-3.83 eV}$$

$$\rightarrow NO^+ (^1\Sigma^+) + H_2 (^1\Sigma_g^+) + H (^2S) \quad \Delta H = \text{-3.26 eV}$$

Figure 41 depicts the absolute cross sections for the ionic products derived from reactions of $O^+ + NH_3$ and ND_3, respectively, at kinetic energies (E_T) in the range from near-thermal to ~15 eV. In the case of the $O^+ + NH_3$ derived from selected ion flow tube (SIFT) thermal rate constant, attributed solely to charge transfer and the average dipole orientation (ADO) model are also shown. The data in Figure 41 indicate that no fewer than four reaction channels occur in these collision systems. The assignments are discussed in greater detail below but it is also worth noting the difficulty in attributing the product ion masses to specific reaction channels resides in the mass coincidences among several prospective products, as well as the primary ion and secondary products.

Reactions with ammonia-d_3 and TOF studies were used to address some of these issues. Two of the observed reaction channels may be assigned unequivocally, in both reaction, a cross section is observed that corresponds to the production a 30 amu product, NO^+. This channel is very small, with a cross section that does not exceed 0.3 Å^2 at any point, and giving rise to no appreciable product below ~7 eV. At the highest energies, the cross section appears to diminish. The other obvious reaction product is H_3O^+, observed clearly only in NH_3 reactions since it is also a small channel and there are no coincident ions (for ND_3 reaction, D_3O^+ coincides with ND_4^+, a secondary product). The H_3O^+ cross section is observed only at low collision energy, where it drops sharply from ~0.8 Å^2 to negligible levels with increasing energy.
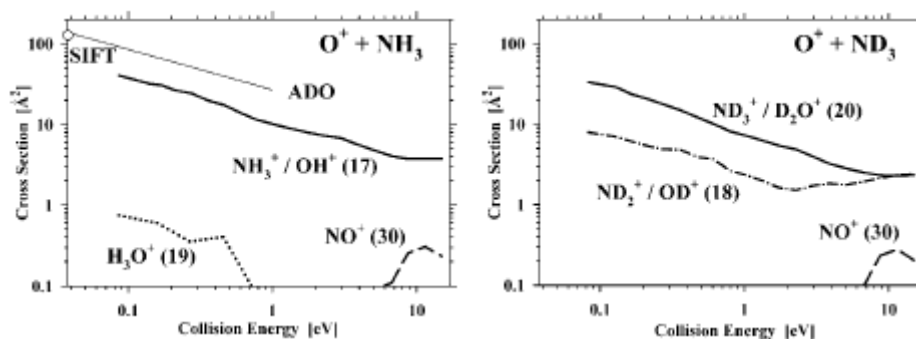

Figure 41: Absolute Cross Sections for $O^+ + NH_3(ND_3)$

The largest cross sections in Figure 41 involve ion products of 17 and 20 amu, respectively. The early SIFT work on normal ammonia would suggest that these correspond to charge transfer, and the energy dependence of these cross sections, with a sharp decline with energy at low collision energies and a leveling off at higher E_T is typical of exothermic charge

transfer in polyatomic systems. In either case, however, there are coincident ions, namely OH^+ and D_2O^+, respectively, which are discussed below. At low energy, the NH_3^+/OH^+ cross section is ~40 $Å^2$, substantially less than the SIFT and ADO results, and decreases until it levels off at a value of 3.7 $Å^2$ above 6 eV. The ND_3/D_2O^+ cross section is ~33 $Å^2$ at low energy and levels off at 2.4 $Å^2$ at higher energy. The remaining cross section, observed in ND_3 reactions, involves product ions of mass 18 amu, possibly ND_2^+ and/or OD^+.

The velocity distributions of the 17 and 20 amu product ion are shown for the $O^+ + NH_3$ (ND_3) collisions, respectively, at selected collision energies. The obtained distributions indicate that NH_3^+/OH^+ are scattered in both the forward and backward directions. The dominant peak at low laboratory velocity in each spectrum corresponds to ions with essentially thermal velocity distributions. The small forward scattered component diminishes at higher collision energy. The 2.58 eV plot includes a second velocity distribution (dashed curve) obtained for the same product(s) with a low octopole trapping potential, U_{RF} (~10 V_{rms}, as compared to 100 V_{rms} normally). This TOF spectrum, which is scaled so that the high velocity edge overlaps the same region in the normal spectrum, exhibits a pronounced drop in relative intensity in the region near V_{CM}, indicating that the missing signal, due to ions not retained by the lower trapping field, is the result of wide-angle scattering as opposed to products associated with low recoil velocities in the CM frame.
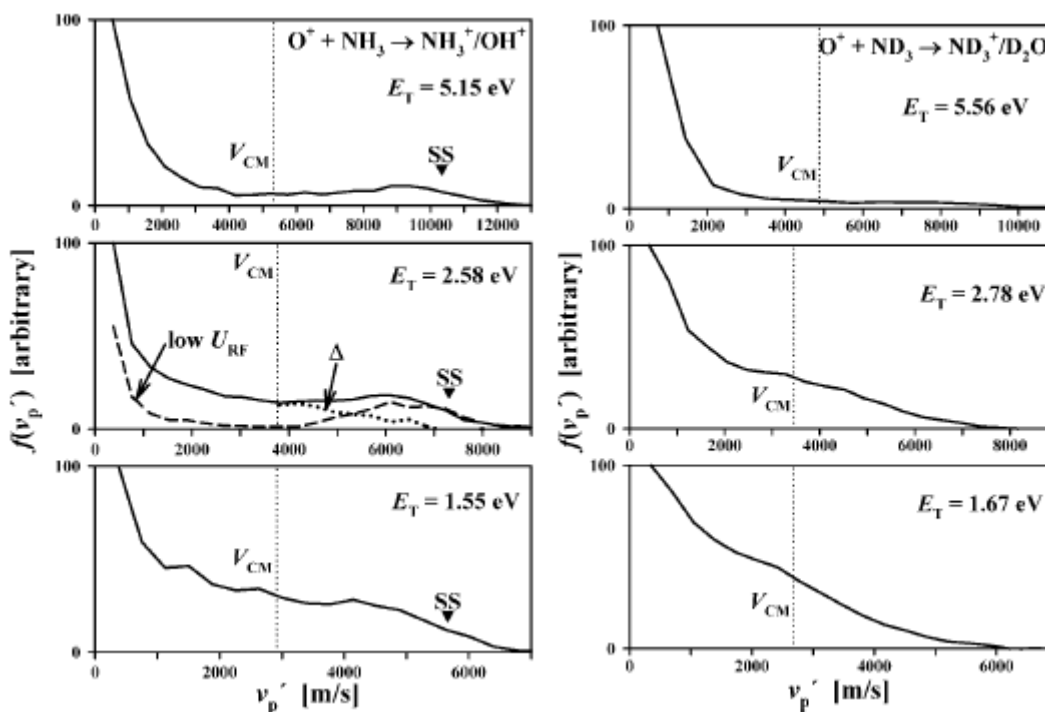

Figure 42: LAB Velocity Distribution for NH_3/ND_3 Product of $O^+ + NH_3/ND_3$

The velocity distributions for the $O^+ + ND_3$ collision system product at 20 amu were obtained in experiments at the same laboratory ion beam energies. The TOF spectra of the mass 20 amu ammonia-d_3 products, ND_3^+/D_2O^+, are similar to those in the NH_3 case. The most remarkable difference being the slight peak in the forward scattered components in the NH_3 particularly evident at velocities just greater than 6000 and 9000 m/s in the data at $E_T = 2.58$ and

5.15 eV, respectively. Given that the H_2O^+/D_2O^+ channel is negligible, and that the data in the two sets are otherwise similar, it is reasonable to consider whether this forward-scattered component corresponds to OH^+. Efficient formation of OH^+ at higher collision energies would be most likely to occur in a stripping mechanism, resulting in forward-scattered product ions. The triangles in each frame of the NH_3 TOF data indicate the nominal spectator stripping (SS) velocity; the SS model represents a limit of the stripping mechanism characterized by an association reaction between the incident ion and the transferred atom.

If the forward scattered peak observed in the $O^+ + NH_3$ data presented in Figure 42 is in part due to OH^+ formation, the low-U_{RF} data at $E_T = 2.58$ eV may be used to determine an upper limit of contribution of OH^+ formation to the 17 amu cross section for the $O^+ + NH_3$ system at this collision energy. The forward-scattered low-U_{RF} component represents 20% of the integrated velocity spectrum obtained at normal U_{RF}. The heavy dotted curve in the respective frame, labeled "Δ", is the difference between the two, and exhibits similar tailing to high velocity as seen in the $O^+ + ND_3$ TOF data. Also noteworthy is that no significant forward "superelastic" scattering is observed; the same may be expected in the backward direction for complex-mediated reactions; therefore the absolute cross sections reported above should be substantially affected at low energy by losses in the ion guide due to products with high backward kinetic energy release.

4.14 $Xe^+/Xe^{2+} + NH_3$ Collision System at Hyperthermal Energies

Our interest in the reactions of singly and doubly charged xenon ions with ammonia derives from the need to understand the interaction of Hall effect and ion spacecraft thrusters with the environment and with the contaminant cloud that surrounds spacecraft in low Earth orbit. As discussed previously, the predominant propellant used in electric propulsion systems is xenon. The 12.1 eV ionization potential of Xe is sufficiently large that collisions with most molecular species encountered in the vicinity of the spacecraft will result in efficient charge transfer. At the hyperthermal collision energies consistent with thruster plume interactions, molecular reaction products may have substantial internal excitation, either because charge transfer is dominated by long range interactions in which all the exothermicity is accommodated in internal modes or because of substantial translational to internal energy conversion in collisions at smaller impact parameters. Hall effect thrusters generate as much as 10% of doubly charged xenon, the reactions of which involve similar considerations. In this section, the ion product distribution and absolute charge exchange cross section after collision of xenon ions with ammonia at hyperthermal energies is considered. The results of this investigation was also the subject of a full length journal article. As such, only the important results and conclusions are discussed below and the interested reader is directed to the full length article containing the remainder of the work in this area.[11] The experimental measurements discussed below were acquired on the instrument described in section 3.2.

Absolute cross sections are obtained by integrated the signal intensities for product and transmitted primary ions and applying the Lambert-Beer expression. Measurements are corrected for reactions resulting from the portion of the residual target gas pressure in the vacuum chamber that resides inside the total octopole volume, amounting typically to ~10% of the measure signals. The total cross sections were measured at low mass resolution, to avoid discrimination in the quadrupole mass filter between fast, heavy primary ions and slow, lightweight product ions. Product branching ratios were obtained at high mass resolution, and were determined by

extrapolating to zero pressure from measurements at two target pressures, to account for secondary reactions.

Figure 43 presents the energy dependence of observed product ions for reactions of Xe^+ + NH_3 and Xe^{2+} + NH_3. For Xe^+ + NH_3, the data are dominated by the charge transfer cross section, which decreases from 200 $Å^2$ at low energies to ~12 $Å^2$ at the highest energies studied. The charge transfer cross section has an $E_T^{-1/2}$ dependence and is consistent with the ADO model. The small NH_2^+ cross section, < 0.5 $Å^2$, is observed at collision energies above 7 eV. The threshold behavior of this channel is consistent with an endothermic channel. Owing to the small NH_2^+ cross section, the effort to accurately determine the energetic threshold for this channel was not made.

As the energy increases from the low energy extreme, the total Xe^{2+} + NH_3 cross section exhibits a sharp fall from its largest value of ~160 $Å^2$ to a minimum of 55 $Å^2$ at ~0.3 eV, and then increases to a maximum of 82 $Å^2$ at 0.7 eV before decreasing and leveling off to ~40 $Å^2$ at the higher energies examined. The ADO model curve is also shown, and is substantially larger than the total Xe^{2+} + NH_3 cross section at energies below the local maximum, above which the cross section is nearly as large as the model. Three Xe^{2+} reaction channels are observed, of which the NH_2^+ product comprises the largest fraction of the total cross section and accounts for nearly all of the increase in the total cross section above the observed minimum. The NH_2^+ cross section decreases from 80 $Å^2$ to the minimum of 30 $Å^2$, then rises to the maximum of 63 $Å^2$ and tails off to ~ 32 $Å^2$. The charge transfer cross section is as large as the NH_2^+ cross section at the low energy extreme, and falls off essentially monotonically to ~8 $Å^2$ at the highest energies. A small NH^+ cross section appears at ~10 eV collision energy and rises to 1 $Å^2$; as with the small NH_2^+ cross section in the Xe^+ + NH_3 data, the energetic threshold for this channel was not determined.
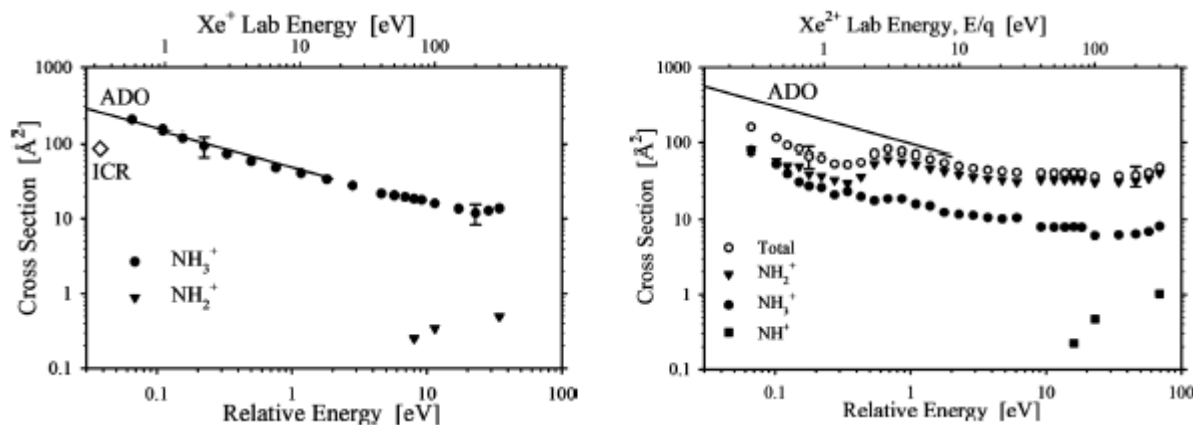

Figure 43: Absolute Cross Sections for the Xenon-Ammonia Collision Systems

The laboratory velocity distributions for both the NH_3^+ (left) and NH_2^+ (right) product ions of the Xe^{2+} + NH_3 collision are depicted in Figure 44 at selected collision energies. We begin first by considering the a-d panels of the NH_3^+ product. At the lower energies the scattering is dominated by a large component at the lowest laboratory velocities, and includes an already small forward contribution that diminished further with increasing collision energy, consistent with a complex-mediated process. In the distributions for all but the lowest energy (b-d) there is an additional feature: a shoulder that comprises back-scattered ions from collisions in which substantial conversion of kinetic to product internal energy occurs. The simulated

distributions in (b) and (d) are for backscattered charge transfer product resulting from direct reaction with ΔE_T = -0.8 and -7.2 eV, respectively.

The velocity distributions for the NH_2^+ product were obtained at the same collision energies and the distributions show general similarity except that the forward-scattered, complex-mediated contribution is substantially larger for NH_2^+ at the lowest collision energy (a), and the high velocity shoulders at higher energy comprise larger fractions of the distributions. The location of the peak in the forward-scattered component at low energy (a) indicates superelastic product recoil; the peak location coincides with ΔE_T = 0.65 eV. The simulation in (b) again for "slow" backward contributions to the NH_2^+ velocity distributions, featuring the same ΔE_T = -0.8 eV as for the NH_3^+ product at the same collision energy. The small amount of forward-scattered intensity in (b) is also superelastic, and clearly contrasts with the behavior of the slow backward component, indicating that these contributions arise from different processes, or via different internal product states arising in the collision complex.
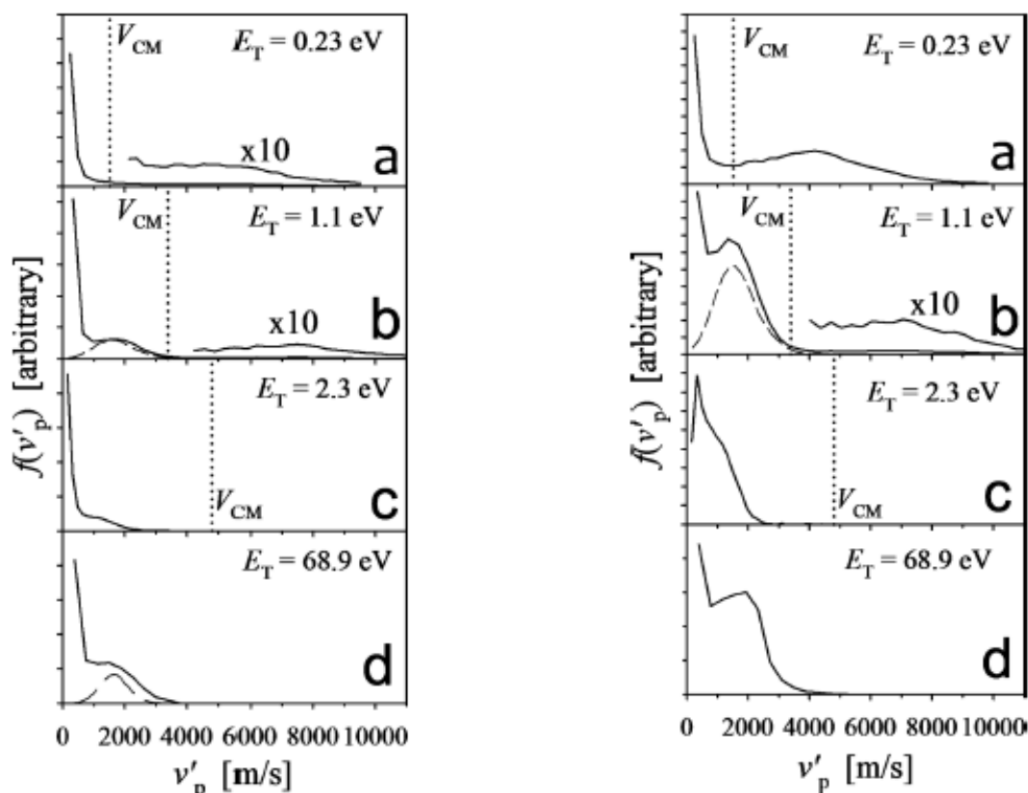

Figure 44: Velocity Distributions of the NH_3^+ and NH_2^+ Product of Xe^{2+} + NH_3

4.15 Optical Emissions of the Xe^+/Xe^{2+} + N_2 Collision System

As discussed in earlier section, measurement of the emission excitation cross sections relevant to ion thrusters can provide a wealth of information. One likely contaminant that can be encountered in low Earth operation of an ion thruster is collision of high velocity xenon ions with thermal nitrogen molecules. In fact, measurements of rare gas ion collisions (of which xenon is a member) with molecular nitrogen has served as experimental underpinning for theoretical benchmarks of ion-molecule charge-transfer dynamics. Ion-molecule reactions offer significant advantages in terms of translational and electronic energy control and have resulted in

fundamental insights into how non-adiabatic effects manifest themselves in vibrational state-to-state dynamics. In this section, energetic xenon ions of kinetic energy E_T are collided with a thermal target gas composed of molecular nitrogen. Optical emissions in the 300-1000 nm range that result are measured for a range of ion-thruster relevant kinetic energies. The work in this section is the subject of a full length journal article and only the most important results and conclusions will be presented here. Interested readers are encouraged to seek out the full journal article for a complete discussion of all experimental findings and results. [15] The experimental work described here uses the apparatus described in section 3.3.

Collisions of $Xe^+ + N_2$ only result in the formation of atomic nitrogen in at collision energies above 20 eV in the center of mass frame. These emissions are most evident in the NIR around 860-875 nm. These emissions increase linearly with increasing collision energy and the integrated emission excitation cross section for all atomic N lines between 854 and 873 nm is approximately 0.025 Å^2 at 110 eV in the center-of-mass frame.

The collisions of $Xe^{2+} + N_2$ result in significantly more rich optical emissions. Figure 45(a) depicts the luminescence spectra obtained at collision energies of 17.6 and 316 eV in the center-of-mass reference frame. The most intense emissions are those in the blue region of the visible spectrum and are assignable to emissions from the N_2^+ (B) state back to the N_2^+ ground state. The most significant of these occurs at 391.4 nm. Also evident in the emission spectrum are the vibrational transitions in the NIR assignable to the N_2^+ (A) state radiatively decaying to the ground N_2^+ electronic state. In Figure 45(b) and (c), zoomed in depictions of the two electronic states are presented. Since nitrogen is molecular, a vibrational progression is observed where each band can be assigned to a specific Δv series. A $\Delta v=-1$ means that the vibrational quantum number increases by 1 as the state decays from the upper electronic state to the lower electronic state. Unfortunately, the optical range of the camera only allowed imaging of the positive bands of the N_2^+ (A-X) transition and did not include the $\Delta v = 0$ transitions, in which the vibrational quantum number is unchanged. The red trace in (b) and (c) is from a scaled (by eye) $Xe^{2+} + Xe$ luminescence spectrum at the same laboratory energy.
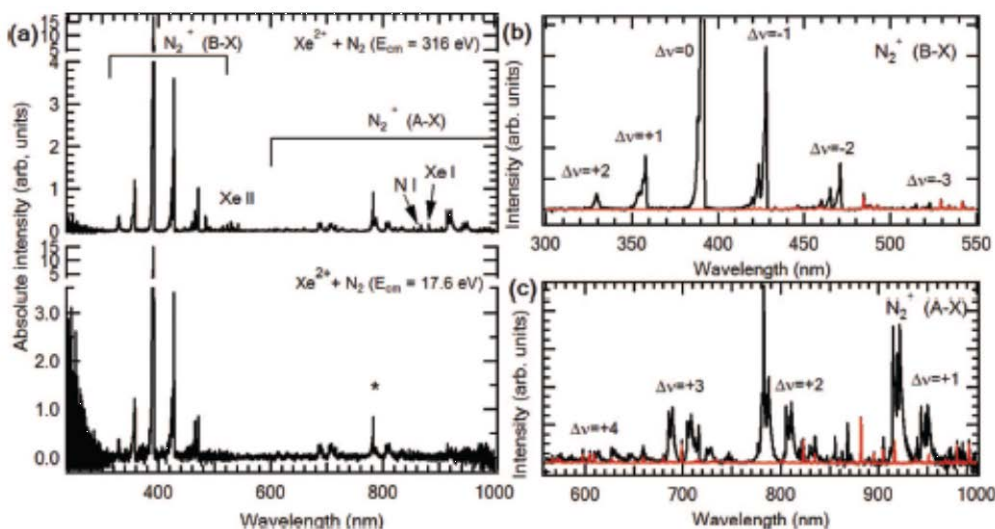

Figure 45: Luminescence Spectra of $Xe^{2+} + N_2$ at Selected Energies

To determine emission excitation cross sections for specific molecular bands associated with a specific vibrational transition within an electronic manifold of transitions, and to derive nascent product state populations, spectral simulations are conducted using the software package

DIATOMIC. These simulations consisted of generating a basis set of individual functions for each vibrational transition observed in the spectra. Molecular constants for N_2^+ and its excited states were obtained from several sources. The best fit coefficients were then used to determine the population of each upper state in an electronic band using the following equation:

$$P(v') = \frac{Z\lambda_{v',v''}^4}{FR_e^2 q_{v',v''}},$$

(19)

where $P(v')$ is the population of the emitting vibrational state, Z is the best fit basis coefficient, F is a proportionality constant that is identical for all transitions in an electronic band, $\lambda_{v',v''}$ is the wavelength of the emission in nm, R_e is the average electronic transition moment, and $q_{v',v''}$ is the Franck-Condon factor for the transitions (v', v''). $P(v')$ and F were varied to minimize the difference between the predicted Z and best fit Z, subject to the constraint that the sum of the populations of the emitting states of an electronic state equals unity and that only one F factor could be employed for the analysis.

This analysis was applied to the N_2^+ (A-X) emissions measured at selected collision energies and the results are reported in Figure 46. At low collision energies, the experimental distribution deviates from the predicted FC distribution and has considerable population in $v = 3$ and 4. At the highest energy of 316 eV, the population distribution is very similar to the FC distribution. A 300 K Boltzmann rotational distribution provided the best agreement with the observed data. The $v = 0$ population was not shown since it was not measured. The FC distribution was normalized such that $v = 1$-7 summed to unity.
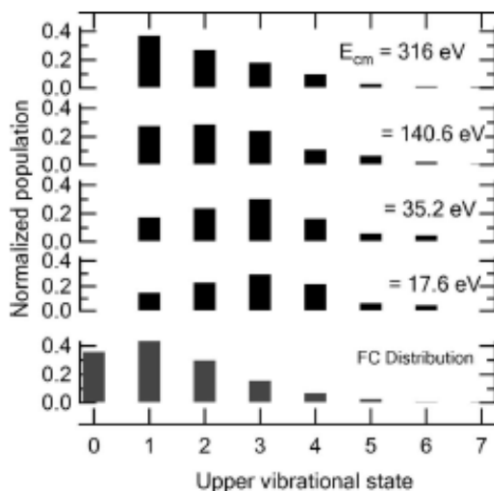

Figure 46: N_2+ Vibrational State Populations Derived from Simulation

The N_2^+ (A-X) vibrational states at low collision energies significantly deviate from the Franck-Condon distribution. At high energies, they mimic the expected distribution. Previous experimental results in this lab and others have noted that charge exchange cross sections of doubly charged species are typically largest for cases where the Coulomb potential and the long-range ion-induced dipole potentials cross at 4 Å. Figure 47 shows the application of this procedure to the electronic states measured in this work. The solid black curve is the ion-induced potential for the spin-orbit state of Xe^{2+} that brings a crossing the closest to 4 Å. The colored and dashed lines are the Coulombic repulsive term for the various vibrational states of the respective electronic states (N_2^+ (A) and N_2^+ (B)) respectively. A vertical dashed line at 4 Å

indicates the desired intersection point. As can be seen in Figure 47(a), this occurs for the $v = 4$ state and in 47(b), the $v = 0$ state of N_2^+ (B).
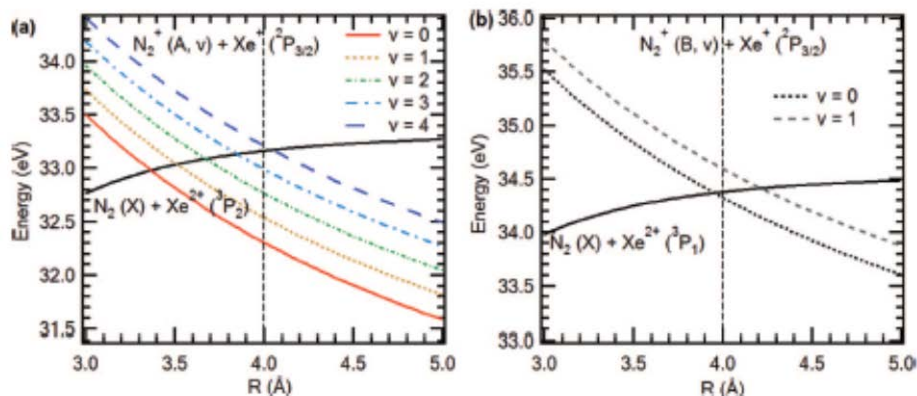

Figure 47: Vibronic Curves of $Xe^{2+} + N_2$

The total integrated cross section of the N_2^+ (A-X) and N_2^+ (B-X) for the $Xe^{2+} + N_2$ over the entire sampled energy range is shown in Figure 48. The (A-X) is truncated because of the inability to collect the optical emissions above 1000 nm. The cross section values are effectively constant above 40 eV in the center-of-mass reference frame. The value of the B-X transition decreases from 4 $Å^2$ at the lowest energies to ~3 $Å^2$ while the *lower limit* of the A-X transition increases from 0.4 $Å^2$ to 1 $Å^2$ over the same energy range.
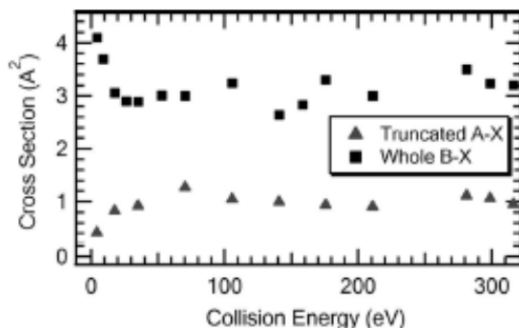

Figure 48: Emission-excitation Cross Section for the A-X and B-X Transitions of N_2^+

5. CONCLUSIONS

Key findings from basic research investigations pursued by the Space Chemistry Laboratory over the previous eight years have been reported. The research efforts have focused on improving the fundamental understanding of the physics of electrospray propulsion, measurement and interpretation of the fundamental physics of the plasma environment typical of Hall effect thrusters and processes typical of ion thrusters, and understanding the chemistry of important atmospheric/contamination hazards associated with electric propulsion systems.

REFERENCES

[1] Chiu, Y.H., et al., *Vacuum electrospray ionization study of the ionic liquid, [Emim][Im],* International Journal of Mass Spectrometry, 2007, **265**(2–3), pp. 146-158.

[2] Luedtke, W.D., et al., *Nanojets, Electrospray, and Ion Field Evaporation: Molecular Dynamics Simulations and Laboratory Experiments,* The Journal of Physical Chemistry A, 2008, **112**(40), pp. 9628-9649.

[3] Brian, T., M. Shawn, and C. Yu-Hui, *Mass Spectrometric Analysis of the Electrospray Plume from an Externally Wetted Tungsten Ribbon Emitter*, in *45th AIAA/ASME/SAE/ASEE Joint Propulsion Conference & Exhibit,* 2009, American Institute of Aeronautics and Astronautics.

[4] Brian, T., et al., *Effect of Aspect Ratio on the Wettability and Electrospray Properties of Porous Tungsten Emitters with the Ionic Liquid [Emim][Im]*, in *46th AIAA/ASME/SAE/ASEE Joint Propulsion Conference & Exhibit,* 2010, American Institute of Aeronautics and Astronautics.

[5] Miller, S.W., et al., *Electrospray of 1-Butyl-3-Methylimidazolium Dicyanamide Under Variable Flow Rate Operations,* Journal of Propulsion and Power, 2014, **30**(6), pp. 1701-1710.

[6] Prince, B.D., et al., *Molecular Dynamics Simulations of 1-Ethyl-3-methylimidazolium Bis[(trifluoromethyl)sulfonyl]imide Clusters and Nanodrops,* The Journal of Physical Chemistry A, 2015, **119**(2), pp. 352-368.

[7] Chiu, Y.H., et al., *Large-angle xenon ion scattering in Xe-propelled electrostatic thrusters: differential cross sections,* Journal of Physics D: Applied Physics, 2008, **41**(16): p. 165503.

[8] Hause, M.L., B.D. Prince, and R.J. Bemish, *Krypton charge exchange cross sections for Hall effect thruster models,* Journal of Applied Physics, 2013, **113**(16), p. 163301.

[9] Hause, M.L., B.D. Prince, and R.J. Bemish, *A guided-ion beam study of the collisions and reactions of I+ and I2+ with I2,* The Journal of Chemical Physics, 2015, **142**(7), p. 074301.

[10] Levandier, D.J., Y.-H. Chiu, and R.A. Dressler, *A Guided-Ion Beam Study of the O+(4S) + NH3 System at Hyperthermal Energies†,* The Journal of Physical Chemistry A, 2008, **112**(39), pp. 9601-9606.

[11] Levandier, D.J. and Y.-H. Chiu, *A guided-ion beam study of the reactions of Xe+ and Xe2+ with NH3 at hyperthermal collision energies,* The Journal of Chemical Physics, 2010, **133**(15), p. 154304.

[12] Sommerville, J.D., et al., *Ion-Collision Emission Excitation Cross Sections for Xenon Electric Thruster Plasmas,* Journal of Propulsion and Power, 2008, **24**(4), pp. 880-888.

[13] Rainer, A.D., et al., *Near-infrared collisional radiative model for Xe plasma electrostatic thrusters: the role of metastable atoms,* Journal of Physics D: Applied Physics, 2009, **42**(18), p. 185203.

[14] Prince, B.D., R.J. Bemish, and Y.-H. Chiu, *Emission-Excitation Cross Sections Relevant to Krypton-Propelled Electric Thrusters,* Journal of Propulsion and Power, 2014, **31**(2), pp.725-736.

[15] Prince, B.D. and Y.-H. Chiu, *Luminescence measurements of Xe+ + N2 and Xe2+ + N2 hyperthermal charge transfer collisions,* The Journal of Chemical Physics, 2011, **135**(10), p. 104308.

[16]   Gamero-Castaño, M. and J. Fernández de la Mora, *Direct measurement of ion evaporation kinetics from electrified liquid surfaces,* The Journal of Chemical Physics, 2000, **113**(2), pp. 815-832.

[17]   Miller, J.S., et al., *Xenon charge exchange cross sections for electrostatic thruster models,* Journal of Applied Physics, 2002, **91**(3), pp. 984-991.

[18]   Paidarová, I. and F.X. Gadea, *Accurate ab initio calculation of potential energy curves and transition dipole moments of the Xe2+ molecular ion,* Chemical Physics, 2001, **274**(1), pp. 1-9.

[19]   Walhout, M., A. Witte, and S.L. Rolston, *Precision measurement of the metastable 6 \textit{s} [3/2${]}_{2}$ lifetime in xenon,* Physical Review Letters, 1994, **72**(18), pp. 2843-2846.

[20]   Karabadzhak, G.F., Y.-h. Chiu, and R.A. Dressler, *Passive optical diagnostic of Xe propelled Hall thrusters. II. Collisional-radiative model,* Journal of Applied Physics, 2006, **99**(11), p. 113305.

[21]   Jung, R.O., et al., *Electron-impact excitation cross sections from the xenon $J=2$ metastable level,* Physical Review A, 2005, **72**(2), p. 022723.

[22]   Chiu, Y.-h., et al., *Passive optical diagnostic of Xe-propelled Hall thrusters. I. Emission cross sections,* Journal of Applied Physics, 2006, **99**(11), p. 113304.

[23]   Brian, B., G. Alec, and H. William, *The Effects of Clustering Multiple Hall Thrusters on Plasma Plume Properties*, in *39th AIAA/ASME/SAE/ASEE Joint Propulsion Conference and Exhibit,* 2003, American Institute of Aeronautics and Astronautics.

[24]   Aymar, M. and M. Coulombe, *Theoretical transition probabilities and lifetimes in Kr I and Xe I spectra,* Atomic Data and Nuclear Data Tables, 1978, **21**(6), pp. 537-566.

[25]   Kalus, R., et al., *Modelling of Krn+ clusters (n=2–20). I. Structures and energetics,* Chemical Physics, 2003, **294**(2), pp. 141-153.

[26]   Sun, L. and G.C. Schatz, *Direct Dynamics Classical Trajectory Simulations of the O+ + CH4 Reaction at Hyperthermal Energies†,* The Journal of Physical Chemistry B, 2005, **109**(17), pp. 8431-8438.

[27]   Levandier, D.J., et al., *Hyperthermal Reactions of O+(4S3/2) with CD4 and CH4: Theory and Experiment†,* The Journal of Physical Chemistry A, 2004, **108**(45), pp. 9794-9804.

LIST OF ACRONYMS

AC	Alternating Current (electrical)
AFRL	Air Force Research Laboratory
AFSPC	Air Force Space Command
CCD	Charge coupled device
CRM	Collisional Radiative Model
DC	Direct Current (electrical)
FC	Faraday Cup
GIB	Guided ion beam (apparatus)
INCLUDE	Ion-neutral chemi-luminescence detector (apparatus)
MD	Molecular Dynamics
MP2	Moller-Plesset second order perturbation theory
QCM	Quartz Crystal Microbalance
QM	Quantum Mechanical
RPA	Retarding Potential Analyzer

DISTRIBUTION LIST

DTIC/OCP
8725 John J. Kingman Rd, Suite 0944
Ft Belvoir, VA 22060-6218   1 cy

AFRL/RVIL
Kirtland AFB, NM 87117-5776   2 cys

Official Record Copy
AFRL/RVBXT/Dr. Raymond Bemish   1 cy

This page is intentionally left blank.